Spring 2016

A Study On The Synthesis And Properties Of Gold Nanoparticles And Their Applications To Surface Enhanced Raman Spectroscopy

Daniel Robert Soden

Follow this and additional works at: https://bearworks.missouristate.edu/theses

🔥 Part of the Materials Science and Engineering Commons

Recommended Citation

A STUDY ON THE SYNTHESIS AND PROPERTIES OF GOLD NANOPARTICLES AND THEIR APPLICATIONS TO SURFACE ENHANCED RAMAN SPECTROSCOPY

A Masters Thesis

Presented to

The Graduate College of

Missouri State University

In Partial Fulfillment

Of the Requirements for the Degree

Master of Science, Materials Science

By

Daniel Robert Soden

May 2016

A STUDY ON THE SYNTHESIS AND PROPERTIES OF GOLD

NANOPARTICLES AND THEIR APPLICATIONS TO SURFACE ENHANCED

RAMAN SPECTROSCOPY

Physics, Astronomy, and Materials Science

Missouri State University, May 2016

Master of Science, Materials Science

Daniel Robert Soden

ABSTRACT

Surface enhanced Raman substrates represent a critical step in the sensitivity augmentation of Raman spectroscopy, but due to the time and expertise currently required in the synthesis process, they have not been fully realized within an industrial setting. This thesis aims to investigate a new technique in surface enhanced Raman spectroscopy (SERS) substrate fabrication designed to decrease synthesis time and map the most effective growth parameters for a successful Raman intensity boost. Sputter physical vapor deposition was utilized to deposit a gold (Au) layer on an insulating substrate, and annealing treatments were applied to agglomerate the Au atoms into the sought after nanostructures conducive to the SERS effect. Substrates were characterized with a variety of techniques including scanning electron microscopy, Raman spectroscopy, and atomic force microscopy, as well as several others. Physical morphologies of the nano features are summarized as well as their impact upon spectroscopic behavior. Surface enhanced Raman intensity boost is also documented and linked back to growth parameters in order to determine effective deposition methods for a successful SERS substrate.

KEYWORDS: Raman spectroscopy, SERS, localized surface plasmon resonance, metal nanoparticles, sputter physical vapor deposition

This abstract is approved as to form and content

_____

Kartik Ghosh Ph.D
Chairperson
Missouri State University

A STUDY ON THE SYNTHESIS AND PROPERTIES OF GOLD

NANOPARTICLES AND THEIR APPLICATIONS TO SURFACE ENHANCED

RAMAN SPECTROSCOPY

By

Daniel Robert Soden

A Masters Thesis
Submitted to the Graduate College
Of Missouri State University
In Partial Fulfillment of the Requirements
For the Degree of Master of Science, Materials Science

May 2016

Approved:

_____

Kartik Ghosh, PhD

_____

David Cornelison, PhD

_____

Adam Wanekaya, PhD

_____

Julie Masterson, PhD: Dean, Graduate College

ACKNOWLEDGEMENTS

TABLE OF CONTENTS

LIST OF TABLES

LIST OF FIGURES

CHAPTER 1: INTRODUCTION AND BACKGROUND

1.1 Nanotechnology

Just as with the discovery of electricity in the 1700's, the inception of nanotechnology has completely altered the way human beings see the world. The ability to manipulate matter at the nano level has opened up an entirely new world of discovery and application for scientists and engineers to explore and harness. A nanoparticle is loosely defined as a collection of molecules bound together with a radius of less than 100 nanometers (nm), or 10^{-7} meters. However, while this definition makes perfect technical sense, it fails to really encapsulate what it is that makes nanoparticles so revolutionary. Many bulk material properties can be characterized by a measurement over some length. Charles Pool Jr. and Frank Owens use electrical conductivity as an example in their manuscript, "An Introduction to Nanotechnology", and nanoparticle radii typically fall short of that characteristic defining length. In the aforementioned example, electrical conductivity is characterized through the mean free path, or the length that an electron goes between collisions in a solid. Should a nanoparticle's radius fall under that length, previously unstudied physics and chemistry will ensue and may then be studied.[1]

Many methods exist to synthesize nanoparticles, primarily divided between a top-down and bottom-up approach. In any kind of top-down procedure, synthesis of nanomaterials occurs through a breakdown of constituent bulk material. The discovery of graphene perfectly encapsulates this method, using adhesive tape to pull layers of graphene from bulk graphite.[2] Inversely; bottom-up synthesis involves self-assembling systems that combine to form nanoparticle arrays.[3] This approach shows the most

promise for innovation, as it allows for different materials to be combined on the nanoscale, something that has previously been impossible. Primary growth methods include pulsed laser deposition (PLD), chemical vapor deposition (CVD), e-beam epitaxy, and sputtering physical vapor deposition. It is this last technique that is utilized most extensively in this thesis and will be explored in some depth later.

1.2 Gold: Fundamentals and Properties

Standing the test of time as one of the largest financial bulwarks of the last millennia, gold (Au) has risen to become one of the most valued materials mankind has ever discovered. Its incredibly inert structure and ability to endure most any weathering placed upon it shows its ability as much more than just a bartering tool. Gold possesses many interesting qualities that, when utilized properly, make it an incredibly versatile tool with a lot to offer.

As previously mentioned, many bulk materials begin to exhibit previously unreported qualities when broken down into components that exist on the nanolevel, and gold is no exception. As the size of the gold particle shrinks down below that of incident light, very exciting optical properties begin to emerge. A more in depth analysis of this effect will be provided later in this thesis, but these properties have led gold to be used for far more than simply a tool for hoarding draconian wealth. Even as far back as the seventeenth century, small constituents of gold nanoparticles were used in churches as a coloring tool for stained glass windows. The incident light was scattered and appeared red to the human eye, and was thus a very popular technique.[4] Unfortunately, even with use of gold nano-components dating back for hundreds of years, scientists were unable to

make use of these effects until very recently. However, since the advent of nanotechnology and its applications, gold has received its fair share of attention, most notably for its tunable optical features, which will be extensively utilized and discussed at length during this thesis.

1.3 Deposition Dynamics and Crystal Structure Formation

As this thesis deals very extensively with physical vapor deposition, it is beneficial to begin with a basic discussion of crystal structure, basic deposition dynamic, and how they relate to gold's FCC crystal structure, pictured below in Figure 1.1.

: Edge Atoms

: Face Centered Atoms
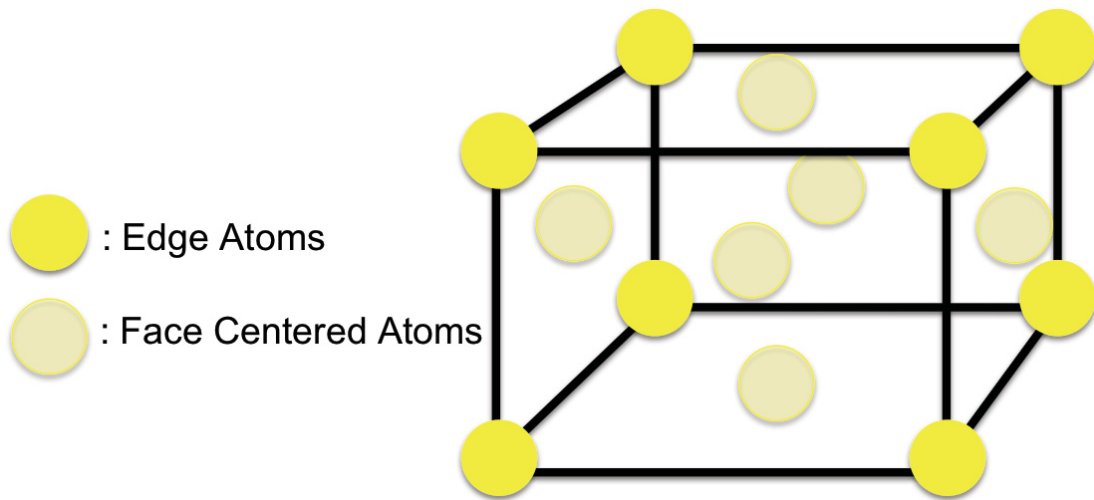
Figure 1.1: Face centered cubic (FCC) gold crystal structure

During the process of thin film growth on a substrate, several fundamental processes occur as atoms first come together at nucleation sites, begin to form islands, coalesce and combine into larger islands, grow polycrystalline structures, form a

continuous structure and began true film growth.[5] During the course of this study, gold will be deposited under a variety of different sputter conditions, resulting in structure formation shown in many different steps of the growth process. These different structure formations will result in radically different nanostructure distribution conditions before and after annealing treatments.

Underlying substrate structure can also play a role in the growth dynamic of thin films as well, and due to the fact that gold was deposited on both silicon and quartz, this is a parameter to keep in mind. Silicon has a face centered diamond structures, potentially promoting more ordered growth parameters, and quartz has a more amorphous structure allowing for more random growth.[6]

1.4 Nanostructure Formation and Dynamics In High Temperature Environments

The melting and boiling points of bulk substances have long been a mainstay within the scientific community, used to calibrate machines and construct experiments based upon material specific temperature ranges. However, it is also relatively well known that these temperatures associated with the various phase changes are based upon the science of averages, and that they are not exact. Put another way, it is important to note that phase change is not an immediate process, rather; it is a gradual, statistical shift that occurs as a material ventures closer and closer to its melting or boiling point. Moreover, once a substance is broken down enough to be classified as a nanomaterial, its phase change dynamics become even more complicated, as the surface area of the material begins to overshadow its volume based characteristics.

As this thesis deals quite extensively in the high temperature dynamics of nanoparticles, it is of high importance to take note of the nature of their phase change processes. In fact, there are two separate processes that affect the size and morphology of formed nanostructures within a significantly heated environment, the transition from solid to liquid, and direct sublimation of material.

First and most obvious is the melting process undergone by solid materials subjected to annealing, or heating. In a study conducted at the National University of Singapore, this process was investigated via analysis of the size of deposited gold nanostructutres versus annealing temperatures. Triangular Au nano-disks were placed on Silicon substrates and annealed a various temperatures between 200°C and 950°C for periods of 30 minutes apiece. As temperature increased and began to approach gold's melting point of 1064°C, these triangular structures began to retract as the thinner, more extended portions of the nanostructure began to experience a certain degree of surface melting. As these ends transition into a more liquid state, the surface tension exhibited by the remaining Au caused the melted portions to move back toward the center of the structure, resulting in a more circular structure.[7] It is important to note that in this process, no gold is lost to atmosphere, resulting in an economical process.

In a like manner, sublimation of the constituent material must also be taken into account when discussing the thermal characteristics of nanomaterials. Although both melting and sublimation will produce roughly the same distribution of nanoparticles seen in Figure 1.2, the distinction between the two processes is especially important as in contrast to a melting process, sublimation of material will result in a less efficient process, as portions of the base material will be lost during particle synthesis.
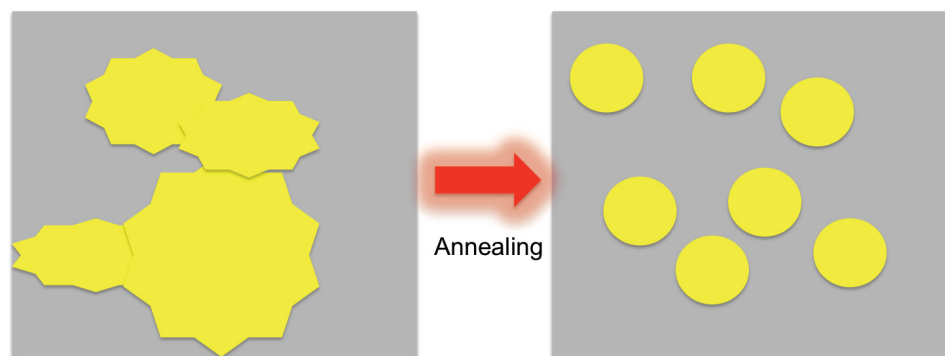
Figure 1.2: Melting dynamics of Au nanoparticles during annealing treatments

Summarized in an article published in Small Communications, researchers from the University of Georgia have delved into the heating dynamics of other noble metals quite extensively. Through studying the sublimation process of silver, Ding et al began to clarify the most energetically favorable surface formed during the annealing process. FCC structured materials like Ag and Au tend to have energetically favorable surfaces with h k l designations such as [1 0 0] or [1 1 0], influencing nanoparticle shape as the sublimation process takes place. Temperatures at which these dynamics begin to take place are reported to be roughly around 50% of silver's bulk boiling point of 2,162°C.[8] Due to the fact that the highest temperature reached in this experiment is 500°C, roughly 17% of gold's boiling point of 2,970°C, sublimation dynamics may be more limited, but due to the relatively unmapped nature of nanoscience, it cannot be ruled out as a possibility.

1.5 Raman Spectroscopy

Pioneered in the late 1920s, Raman spectroscopy represents one of the most effective material characterization tools used today, allowing scientists to identify

constituent elements and bonding dynamics as easily as checking the fingerprint of a human being. To accomplish this, a laser is made incident on a given material under examination, exciting the resident electrons to higher energy levels, creating oscillating phonon modes within the material. As these electrons fall back down and the phonons decrease their energy, the photons ejected from the material as a result are collected via carefully calibrated detectors. As shown in Figure 1.3, an incident photon from the laser can cause several different kinds of scattering modes. Elastic scattering, or Raleigh scattering, occurs when the excited electrons fall back to the same energy level. This produces very little important data, as a scattered photon possessing the same amount of energy as the incident photons allows for no inferences to be made regarding internal system dynamics. Much more interestingly, photons can also scatter in an inelastic manner, know as either Stokes or Anti-Stokes scattering. Stokes scattering will leave the electron in a less excited state than when it began, while Anti-Stokes will leave it in a higher energetic state. Both of these produce energetic shifts that correspond to various kinds of vibrational modes within the material, providing unique identification to various interactions within a material.[9] Unfortunately, these inelastic scattering modes are typically dwarfed by the fluorescent emissions produced by the elastically scattered photons. As elaborated within the polarizability equation, Raleigh scattering is produced from the intrinsic polorizability of the material, while the Stokes and Anti-Stokes are drawn from the polarizability change due to physical position shift. This limits the usefulness of the technique, making a fairly advanced detection and filtering system necessary.

7

Virtual Energy States

hf_{Photon}

hf_{Photon}

hf_{Photon}

$hf_{Photon} - E_0$

hf_{Photon}

$hf_{Photon} + E_0$

1st Excited State E_1

Ground State E_0

Raleigh　　Stokes　　Anti-Stokes

Elastic　　　　Inelastic

Incident Photon

R

S

A
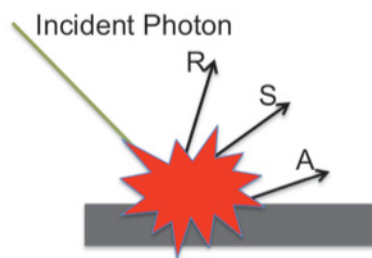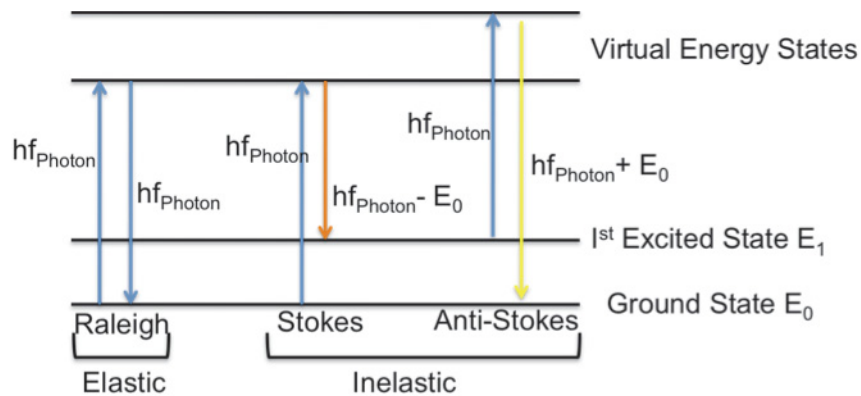
R: Raleigh Scattering
S: Stokes Scattering
A: Anti-Stokes Scattering

$$P = \alpha_0 E_0 \cos(2\pi\alpha_0 t) + \tfrac{1}{2}(d\alpha/dx)_0 \left[\cos((hf_{Photon} - E_0)*t) + \cos((hf_{Photon} + E_0)*t)) \right]$$

Raleigh　　　　　　Stokes　　　　　Anti-Stokes
Scattering　　　　Scattering　　　Scattering

P: Dipole Moment
α: Polarizability
(dα/dx): Change in polarizability due to position changes

Figure 1.3: Raman scattering dynamics and the polarizability equation governing elastic and inelastic scattering

It is important to note, however, that not all vibrational modes are detectable through Raman spectroscopy, only symmetrical modes of vibration. Infrared (IR) spectroscopy is required to detect anti-symmetrical vibrational modes.[10] IR spectroscopy gives rise to certain absorption bands associated with the material, taking in energy for the support of altered molecular structure. Raman is associated with the scattering and re-

emission of incident radiation, as symmetrical atomic changes will oscillate back and forth, allowing for the continuous emission of photons.

1.6 Surface Enhanced Raman Spectroscopy

As previously mentioned, Raman spectroscopy, while it represents one of the best characterization methods for internal material dynamics in use today, is still very limited. This limitation is due to the sensitivity necessitated by the relative weakness of the useful inelastic scattering dynamics when compared to the emissions produced by elastic, or Raleigh, scattering. Moreover, many molecules of interest intrinsically posses a relatively low Raman emission intensity, making their internal dynamics a mystery. In the late 1970's, scientists began to seek ways to combat these discrepencies by augmenting the Stokes and Anti-Stokes inelastic scattering signals.[11] As damage to the material could not be risked by altering it in any way, attention turned to the substrate upon which it was placed, giving rise to the colloquial term surface enhances raman spectroscopy (SERS) substrates.

Unsurprisingly, it comes as no easy task to alter a substrate to passively boost any nearby photon expulsion without damaging the constituent material in the process. Fortunately, plasmonics, a realm of science studying the interactions of light and matter, provided a technique known as localized surface plasmon resonance that could provide just the boost required.

1.6.1 Surface Plasmons. Plasmonics represents one of the most enigmatic fields within investigatory science today, focusing on the increasingly subtle interactions between light and matter, and it is here that the doorway to ultrasensitive detection lies.

9

To understand this interaction, one must first go back to a more basic discussion about the fundamental dielectric properties of materials, modeled in Figure 1.4. A material's dielectric constant, or as it is more commonly known, its relative electrical permittivity, is a measure of how much electrical energy exists between two point charges. A material with a high dielectric constant will actively resist forming an electric field; acting as an insulator, while a material with a relatively low dielectric constant will communicate electron flow very well, working as a conductor. The dielectric constant of a material also possesses an imaginary component, which models the phase dependent component of the dielectric quantity.[12] For materials that possess a negative real component of the dielectric constant, and a very low imaginary portion, such as gold or silver, there exists a special quality known as the surface plasmon resonance effect, activated when the dielectric constant of the material approaches the relationship modeled by the below equation.[13]

$$\varepsilon_{Material} = -2\varepsilon_{Environment}$$

Where ε is the dielectric constant. While several materials possess a resonance frequency at some wavelength along the spectrum, noble metal nanoparticles (MNPs) posses the unique ability to satisfy this dielectric equation within the realm of visible light, giving them the ability to be energized through the monochromatic visible light lasers used in Raman spectroscopy. It is this phenomenon that represents the core of ultrasensitive detection technology, and the key to unlocking the potential of surface enhanced Raman spectroscopy.
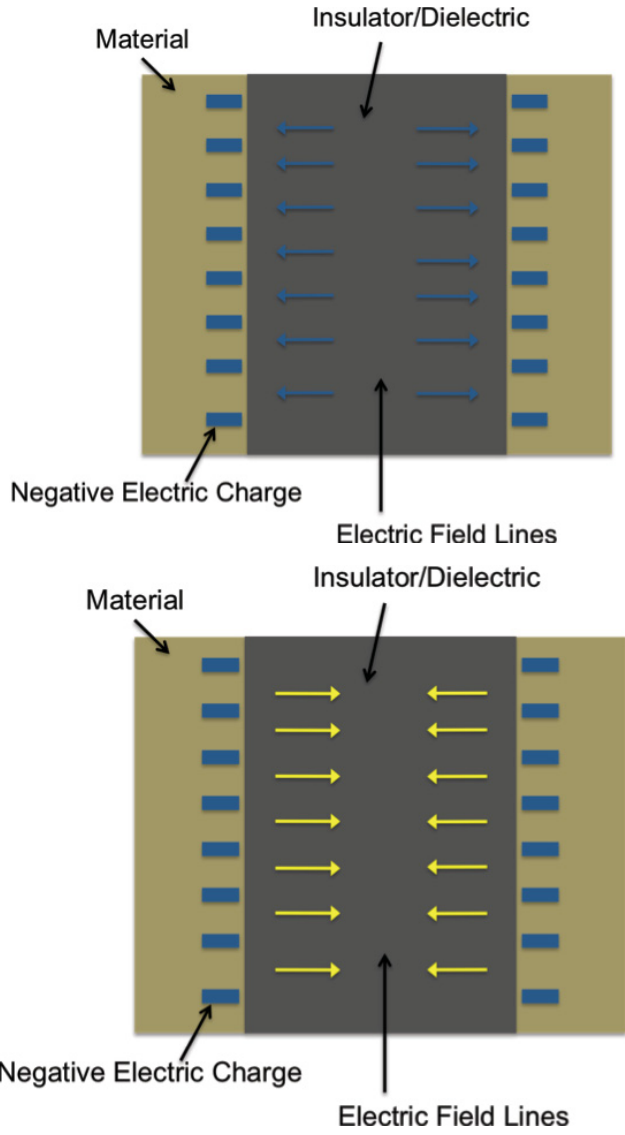
Figure 1.4: The interaction of materials with (a) a positive dielectric constant, and (b) a negative dielectric constant with an insulator

In the case of gold, as is covered in this thesis, light of wavelengths much larger than that of the actual nanoparticle size is made incident upon the patterned gold nanostructures. When the proper wavelength is reached, the electrical energy provided by the incident light forces conduction electrons to oscillate around the nanoparticle, creating a plasmon, shown in Figure 1.5, with a frequency known was the localized surface plasmon resonance (LSPR) frequency. This plasmon brings rise to an electric

field that is related to the resonance frequency.[14] Incident light waves are then trapped close to the surface of the nanoparticle, and experience an intensity boost.[15]
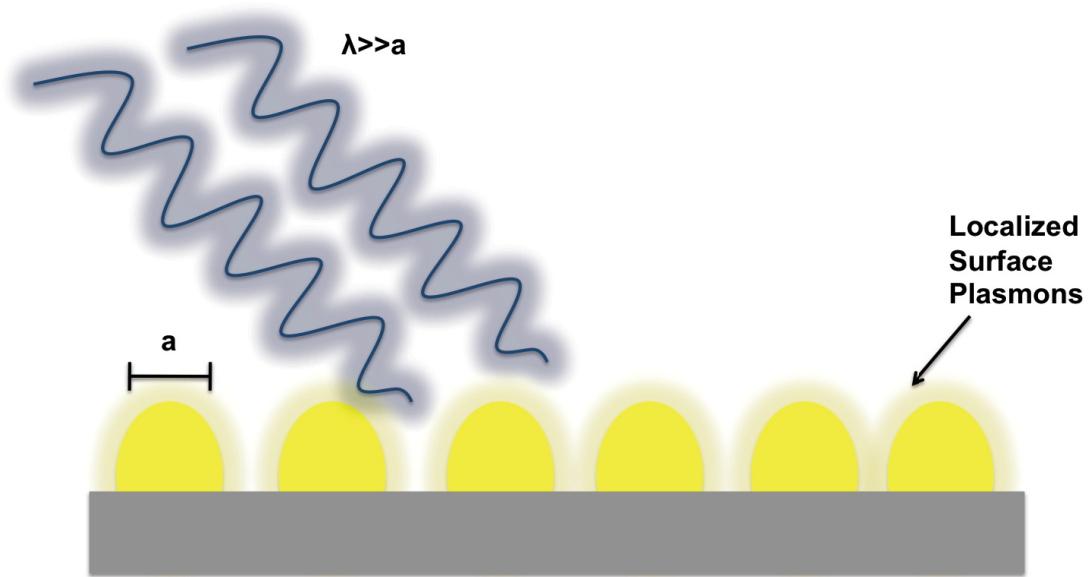
Figure 1.5: Localized surface plasmon resonance effect of incident light of wavelength λ on gold nanoparticles of size λ>>a

To make this phenomenon useful for spectroscopic sensing technology, a closer look at the created electric field must be taken. When the LSPR condition is satisfied, the oscillating plasmon circling the nanoparticle creates a charged environment directly related to the plasmon's resonance frequency. When many of these nanoparticles are placed on an insulating substrate, at relatively close distance to each other, a type of electrically charged array is created along the surface of the insulator. If an analyte material is placed within the electrically charged surface, the energy provided will serve to enhance the intensity of its spectral characteristics. It is this property that serves as the backbone to surface enhanced Raman spectroscopy.

To make the most effective use of the localized surface plasmon resonance effect, several other factors must be taken into account. First, it is not enough to make a noble metal nanoparticle, the size and shape of the structure must also be considered, as this will affect the spectral signature of the LSPR. Thus, synthesis techniques that allow for tuning of size and shape are considered especially valuable and sought after by SERS researchers.

Particle to particle distance also plays an important role in the effectiveness of a SERS substrate, as the oscillating plasmon only extends to a certain distance around the metal nanoparticle. With a closer distance between nanoparticles, plasmonic coupling is also able to take place between the various oscillating phenomena. This coupling allows for the largest created electric fields, and subsequently the most potent SERS intensity boost.[16]

1.6.2 Current Synthesis Techniques. As can be imagined, patterning these golden nanostructures on a substrate is no easy task, and the effort required for many current techniques reflects this difficulty. One such method is the practice of anchoring metallic nanoparticles to a substrate via the application of bifunctional molecules, or molecules that possess not one, but two binding sites. In essence, metal nanoparticles are brought into contact with substrates functionalized with these bifunctional molecules, and are anchored onto the second binding site, creating a patterned SERS substrate. A variety of other methods have been tested for effectiveness; the MNPs can be anchored through an electrostatic interaction, the manipulation of capillary forces, and basic chemical growth, all serve to adhere the nanoparticle for SERS functionalization.[17]

Currently the prime technique for the synthesis of SERS substrates, nanolithography takes the "top-down" approach to substrate synthesis, creating a patterned array of nanoparticles through the use of some kind of chemical mask. Nanolithography is a somewhat broad classification, as there are numerous sub-categories that exist for the technique. Electron beam lithography (EBL) utilizes an electron gun, firing a steady stream of electrons at a resistive film, wearing it away at predetermined spots to create a pattern, allowing for a selective deposition process to take place. While EBL is the most common method of nanolithography, other techniques exist to create a patterned array of MNPs. While nanolithography is typically the most time intensive synthesis method, it is also the most effective in terms of pure SERS signal boost. Lithographic synthesis methods are also popular due to the regularly spaced grids and long range order they supply, providing more of a reliable, predictable boost than other more random techniques.[18]

1.7 Thesis Direction and Statement

As previously elaborated upon, there are several documented synthesis methods for surface enhanced Raman substrates, but many do have one thing in common, the time and effort it takes to furnish a finished product. While current chemical synthesis and nanolithography methods do produce an excellent SERS boost, it does take a reasonable amount of time and a not inconsiderable amount of expertise to synthesize a working substrate.

It is the aim of this thesis to investigate a new synthesis method for SERS substrates focusing on economy and utility of technique. Through the utilization of

14

sputtering physical vapor deposition and a simple annealing step, the complexity of

SERS substrate synthesis can be scaled back considerably, allowing for more utilization

within industrial and medical settings, and unlocking more societal potential of the SERS

effect.

CHAPTER 2: EXPERIMENTAL METHODS

2.1 Experimental Design and Preparation

2.1.1 Experimental Structure. Throughout the course of investigation into this novel SERS substrate synthesis method, several important synthesis variables became apparent. These parameters, summarized below in Table 2.1, were tested and analyzed in a controlled setting to determine each variable's effect on metal nanoparticle synthesis and SERS effectiveness. Variables investigated include the effects of sputter amperage and time and annealing temperature.

Table 2.1: Experimental parameters

Sample Number	Material	Sputter Amperage	Sputter Time	Annealing Temperature
1	Silicon	10 mA	20 Seconds	300 °C
2	Quartz	10 mA	20 Seconds	300 °C
3	Silicon	10 mA	40 Seconds	300 °C
4	Quartz	10 mA	40 Seconds	300 °C
5	Silicon	20 mA	20 Seconds	300°C
6	Quartz	20 mA	20 Seconds	300°C
7	Silicon	20 mA	40 Seconds	300°C
8	Quartz	20 mA	40 Seconds	300°C
9	Silicon	10 mA	20 Seconds	500 °C
10	Quartz	10 mA	20 Seconds	500 °C
11	Silicon	10 mA	40 Seconds	500 °C
12	Quartz	10 mA	40 Seconds	500 °C
13	Silicon	20 mA	20 Seconds	500°C
14	Quartz	20 mA	20 Seconds	500°C
15	Silicon	20 mA	40 Seconds	500°C
16	Quartz	20 mA	40 Seconds	500°C

Analysis on each sample was performed both before and after annealment, gaining data and enabling conclusions to be drawn about the effects of fairly radical changes in synthesis technique to effectiveness. This data will allow for conclusive statements to be made regarding the effect of each parameter on the size and geometry of the constituent gold nanoparticles, as well as to conclusively determine the most economical synthesis method.

2.1.2 Sample Preparation. To ensure no sample contamination and to maintain utmost experimental integrity, great care was taken to sterilize not only the sample substrates, but also the sample boxes and tools used to handle them. Sample preparation proceeded as follows:

1. As each sample will be split into pre and post annealment characterization, 32 sample boxes were prepared and cleaned via acetone.
2. Silicon and quartz samples were cut using the diamond scribe shown in Figure 2.1. They were then soaked and sonicated in acetone (sonication will be discussed more in depth under the equipment section). Each sample was then removed, rinsed under running water, subsequently dipped in de-ionized (DI) water, and finally ethanol before being let sit to dry in air.
3. Samples were then loaded into their respective sample containers to await gold sputter deposition.

Figure 2.1: Diamond scribe used to cut samples

2.2 Equipment

    2.2.1 1510 Sonicator. From cleaning substrates to breaking up bulk material, sonication proves itself as a versatile technique, and one that is prevalent in almost all fields of science. While both bath and probe sonicators do exist, the former, displayed in Figure 2.2, far outnumber

Figure 2.2: BransonIC 1510 ultrasonic bath cleaner

the latter terms of presence within a lab setting, due to the relative superfluous nature of the probe sonicator in terms of power. A bath sonicator more than suffices for cleaning of a substrate, which represents by far the most common use of the machine in practice. Nonetheless, the physics behind both probe and bath sonicators is reasonably similar and simple. In the case of the bath, the metal casing is filled with a liquid, and then vibrates to produce simple mechanical oscillations within the contained liquid. These oscillations produce vacuum bubbles in a process known as cavitation. These vacuum bubbles are

collapsed and destroyed almost as soon as they are created, sending out shockwaves in the form of heat and kinetic energy. This energy acts as a cleaning technique by knocking clear any unwanted contaminates that may be coating the substrate. The effectiveness of this technique can be boosted through the use of a liquid medium such as acetone or ethyl alcohol. In this thesis, each sample was sonicated individually in order to prevent any unwanted abrasion of the substrates.

2.2.2 Ionized Physical Vapor Deposition (Sputtering). Representing the core of this thesis, ionized physical vapor deposition is based around the concept of deposition via the dynamics of kinetic impact. A sample is placed within the sputtering chamber, and a vacuum pump evacuates the chamber of all gaseous contaminants. Once the chamber reaches an appropriate level of vacuum, an inert gas, usually Argon, is pumped into the chamber. The Argon atoms are excited via an electrical field, and eventually ionize, forming the center of the deposition process. As illustrated in Figure 2.3, these ionized atoms are then accelerated via magnetic fields to crash directly into the chosen target, in this case gold, causing portions of the target material to "sputter" off and deposit on the substrate positioned below.[19] Deposition via sputter mechanics is an incredibly useful technique due to the fact that a high level of vacuum is not necessary for function, the target does not need to be heated, and the required Argon gas is relatively inexpensive. The lack of substrate heating is especially important for this investigation, as it prevents the deposited material from forming into a single, uniform film, which would not allow for the proper plasmon dynamics to take place.

19
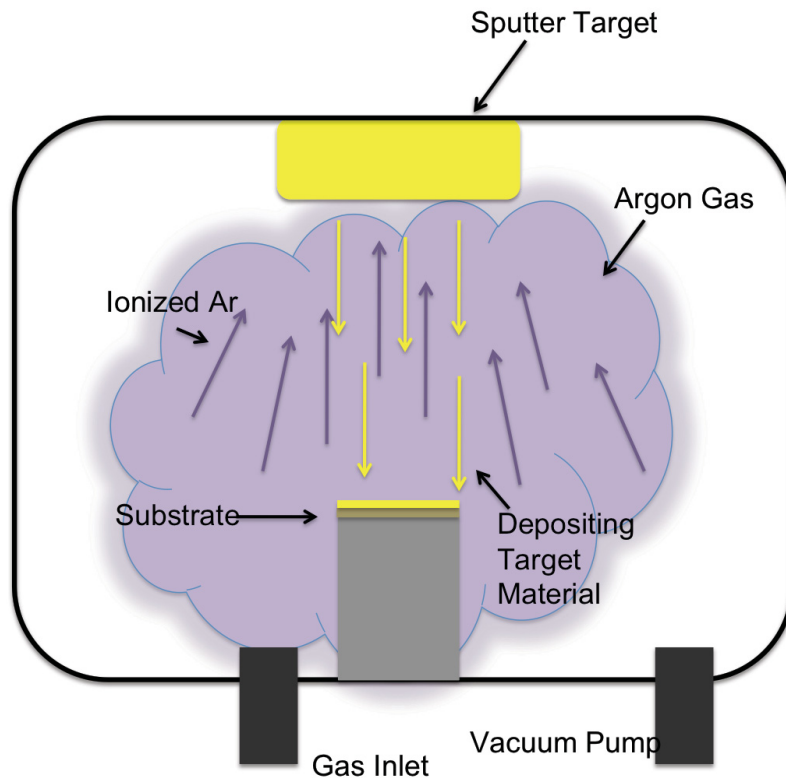
Figure 2.3: Sputter physical vapor deposition dynamics.

The sputter setup used in this thesis can be seen in Figure 2.4. Relatively simple in design, the samples are placed onto a stage inside the chamber, and the system is pumped down to vacuum utilizing the turbo pump seen behind the machine. Argon was then introduced through an access inlet underneath the chamber. Parameters for both sputter time and amperage used are easily altered using the control panel. In this thesis, only an incredibly thin coating is required, and initial testing indicated that amperages of 10-20 mA were acceptable for synthesis. The time of the deposition was varied between 20 seconds and 40 seconds in order to determine optimum conditions for an effective coating.
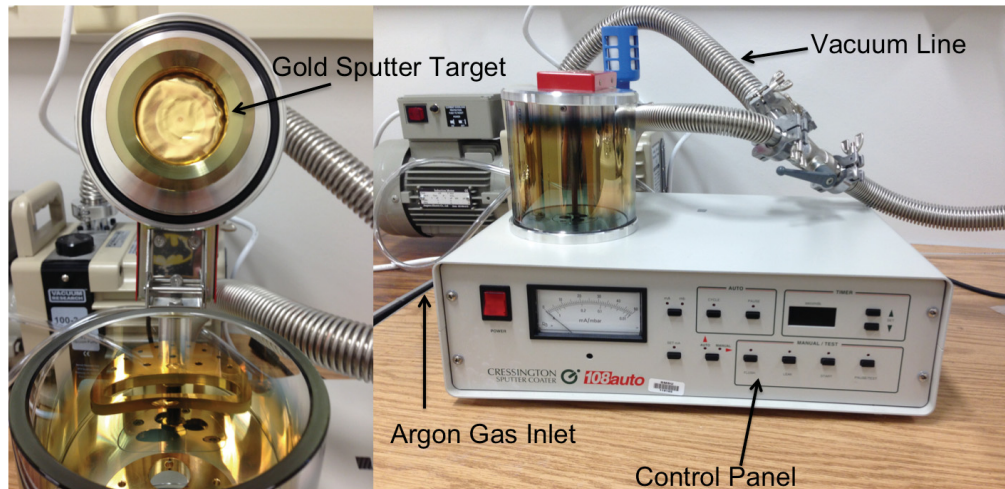
Figure 2.4: Sputter machine, with gold sputter target, vacuum line and pump

2.2.3 Furnace. The furnace in use for this investigation, shown in Figure 2.5, represents one of the simplest machines in popular use for materials synthesis, but ironically, it is also one of
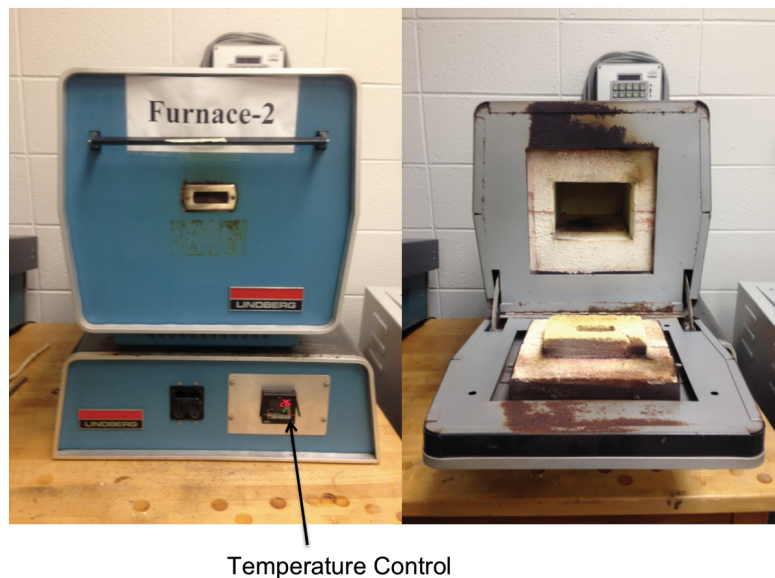
Figure 2.5: Lindberg 51222 Industrial Furnace

the most integral for many applications. During the process of heating a given material on a substrate, or annealing it, typical changes include inducing a certain amount of uniformity to the film, smoothing out aberrations as the melting point of a material draws closer and closer. This process represents the exact antithesis of the dynamics needed to engineer a SERS substrate, however, due to the fact there is so little material deposited during the sputtering process, a different, nano-scale orientated thermal mechanic emerges.

Annealing parameters make up the most interesting aspect of experimental variability in the capstone experiment of this thesis, with temperature being adjustable. In order to facilitate pre and post annealment sample testing, all 16 samples were cut in half with the aforementioned diamond scribe, with one half being annealed according to appropriate parameters, and one half being kept for comparison purposes. To create a strong differential for comparison, annealing temperature was set at both $300°C$ and $500°C$. These rather disparate conditions provided a strong signpost for the type of particle formation dynamics occurring during the annealing process, and allow for strong conclusions to be drawn regarding optimum growth parameters.

Annealing was performed in two different batches, one for each of the temperature settings explored in this investigation. As can be seen in Figure 2.6 (a), all sixteen samples were loaded onto a ceramic dish and positioned into the furnace, already heated to the requisite temperature. Samples were annealed for one hour and then allowed to cool slowly in air before being removed and stored for testing.

Looking to Figure 2.6 (b), color change can already be seen the quartz substrates, showcasing the change in optical properties within the gold film even to the naked eye.
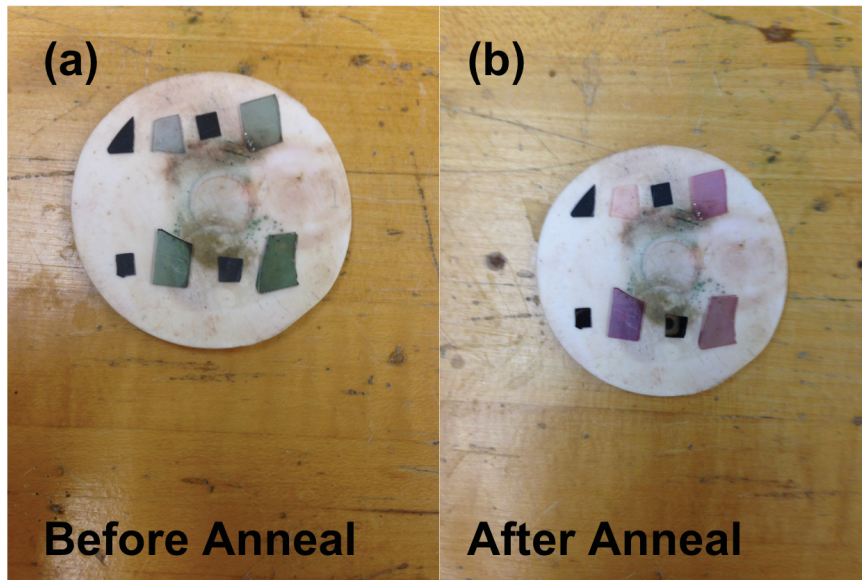
Figure 2.6: Samples 1-8 annealed at 300°C for one hour. Shown (a) before and (b) after annealing treatment

2.2.4 Ultraviolet Visual Spectroscopy. Ultraviolet visual spectroscopy, or uv-vis spectroscopy, measures the wavelengths of light within the ultraviolet and visible spectrums that are transmitted or absorbed by a material in question. As can be seen in Figure 2.7, the ultraviolet visual spectrometer emits light all along the spectrum, being incident on the sample placed on the stand, and displaying the amount of light that is transmitted, communicated via an x-y graph of wavelength versus transmission. This information is very basic, but its importance in the realm of mapping band gaps, and confirming optical properties of materials cannot be overstated. Through a simple calculation, and transference of the data to another graph commonly known as a tauc plot, researchers can map the band gaps of materials in a fairly accurate manner.

In the realm of surface enhanced Raman spectroscopy, ultraviolet visual spectroscopy presents a convenient way to determine the wavelength of light needed to determine the frequency condition required for localized surface plasmon resonance.[20]

When this condition is met, the material will begin to absorb light along the required

spectrum, enabling for accurate determinations regarding the effects of annealing time,

temperature, and particle size on the LSPR condition. As this characterization tool

required light to pass entirely through the studied substrate, only the quartz samples will

be utilized in the test.
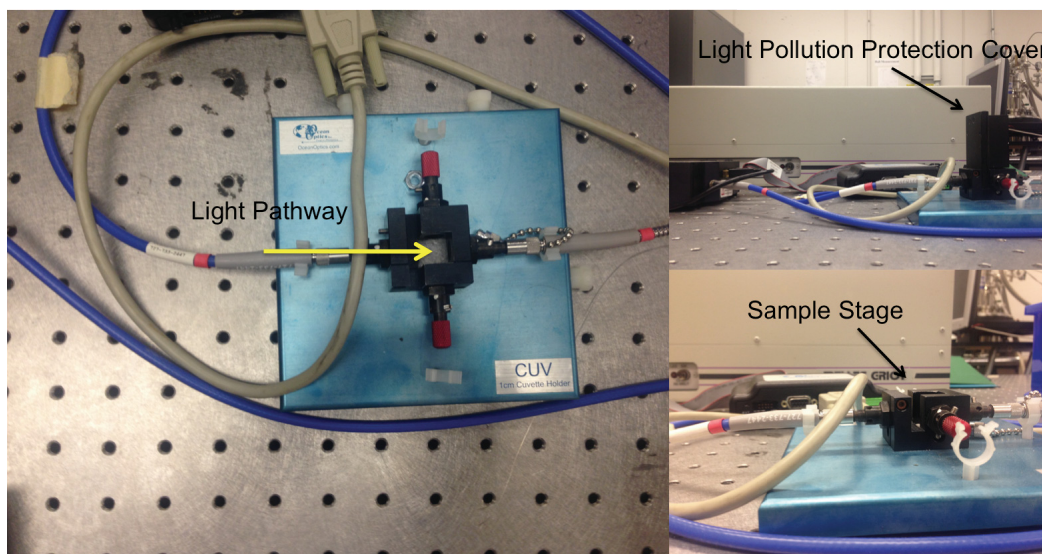
Figure 2.7: Ultraviolet visual (UV-Vis) spectrometer setup

Absorption baselines for this procedure were set using uncoated quartz in order to

provide an accurate measure of increased absorption due to plasmon resonance.

2.2.5 Scanning Electron Microscopy. Microscopy has always been a mainstay

within the scientific community, with the ability to see on a micro level forming the basis

for much of the current understanding of the way the world works. However, following

the advent of quantum mechanics, and as technology becomes focused on smaller and

smaller features and effects, it has become necessary to see with much more clarity into

even the nano realm of reality. This introduces a new set of complications, as most

nanoparticles are much more miniscule than traditional light waves. To combat this, electron based microscopy was born. By bombarding a sample with a steady stream of electrons, controlled and directed via magnetic fields, a backscatter image can be constructed from the scattered particles.[21] This process has allowed scientists to see with their own eyes the dynamics of nanoparticles, opening up a whole new world of analytical possibility, and ensuring the scanning electron microscope (SEM) a place as one of the most effective tools in modern science.

This thesis utilized an FEI Quanta 250 scanning electron microscope, pictured below in Figure 2.8 (a). Samples were prepared as shown in Figure 2.8 (b), placed on top of copper tape before being covered with another piece of copper tape, both to adhere the samples and to ensure electron conductivity, thus bettering image quality. Marks were made to aid in sample
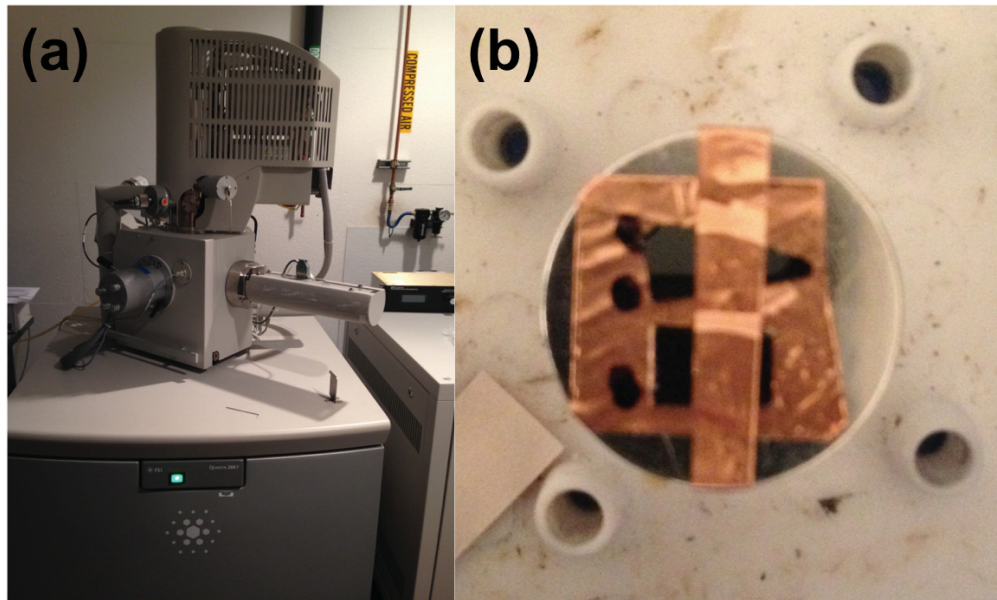
Figure 2.8: (a) FEI Quanta 250 scanning electron microscope, and (b) SEM sample setup with copper conduction tape

identification, one dot indicating a pre-annealed sample, and two dots indicating post-anneal.

Samples were imaged at an 8 mm working distance from the electron source, with a chamber pressure of $6.60 * 10^{-6}$ Torr, an electron gun pressure of $6.65 * 10^{-10}$ Torr, and an emission current of 294 μA. Spot size was kept small at 3.0 mm, while voltage was set at 10.0 kV throughout.

Due to the nature of scanning electron microscopy, creating images based on backscattered electrons, it is something of a necessity to utilize a relatively conductive substrate in order to obtain a high quality, useful image. Unfortunately, this clashes directly with the insulating substrate required for a properly functioning SERS substrate. Initially gold was sputtered onto a Silicon Dioxide (SiO_2) substrate, in hopes that it would provide both a functioning insulator for the SERS effect, and still allow for a reasonable amount of electron mobility for imaging purposes. Unfortunately, the images obtained were far too blurry and vague to obtain useful information about the nanostructures deposited. While the typical solution to this problem would be to sputter deposit a thin layer of carbon or gold on top of the substrate to increase conductivity, this would in turn ruin the substrate's SERS potential, making it a non-option. Instead, the experiment was reformatted to its current form, with base silicon being utilized as a substrate material in place of SiO_2. This allowed for proper imaging to take place, while still keeping the quartz insulator samples pristine for Raman testing of the substrates.

2.2.6 SEM Image Analysis Software (Image J). Compounding the usefulness of scanning electron microscopy, open source image analysis software Image J allows for a

much more quantifiable set of information to be gathered from a grayscale SEM image

through an innovative process of pixel analysis.[22] First, a picture taken with the SEM, and

more importantly, marked with the typical scale bar, is loaded into the program. As

shown in Figure 2.9, the scale bar is then measured in terms of pixel width, and compared

with the actual known width of 1000 nm.
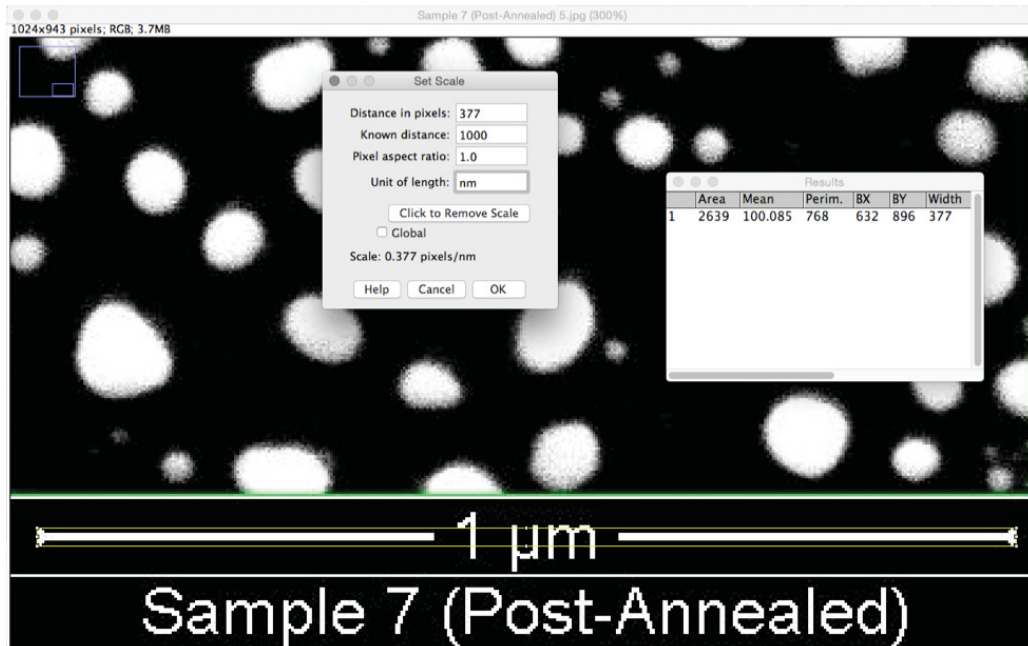
Figure 2.9: Pixel to nanometer normalization procedure of sample 7 post anneal

This allows for all subsequent measurements to be taken in nanometers as

opposed to pixels, making results much more useful. The image is then specified to be 8-

bit, an important distinction, as the program can then prioritize the grayscale and perform

a color threshold calculation. Figure 2.10 depicts the threshold analysis of the image,

specifying which grayscale settings should be included in the black and white contrast

image. The image is then reduced to black and white, cutting of the grayscale pixels at

the indicated wavelength and allowing for the software to distinguish on a pixel-by-pixel basis the difference between particle and background.
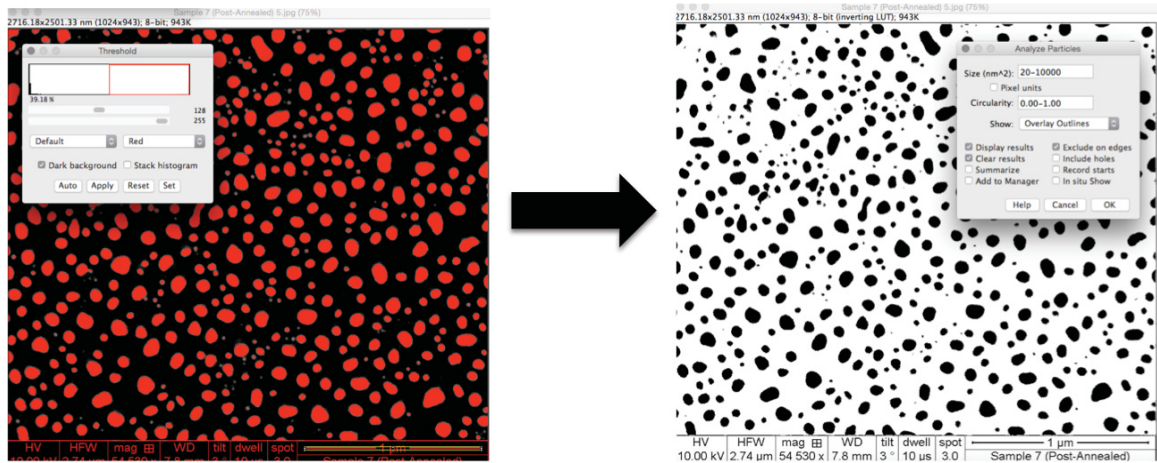
Figure 2.10: Image J SEM color threshold analysis for determination of particle boundaries

Once this black and white image has been generated, it is possible to perform various types of particle analysis, the most relevant to this thesis regarding particle area distribution. Figure 2.11 displays how particles are labeled individually and mapped to a tunable area distribution histogram, this study limiting the area to 20 nm^2 on the low side and 10,000 nm^2 on the upper end. Eccentricity of the analyzed particles was not made a parameter for selection, as many of the particles are of varying shapes. The SERS effect is not limited exclusively to circular particles, so exclusion from analysis based on the degree of particle circularity could have potentially excluded valuable data from the study.
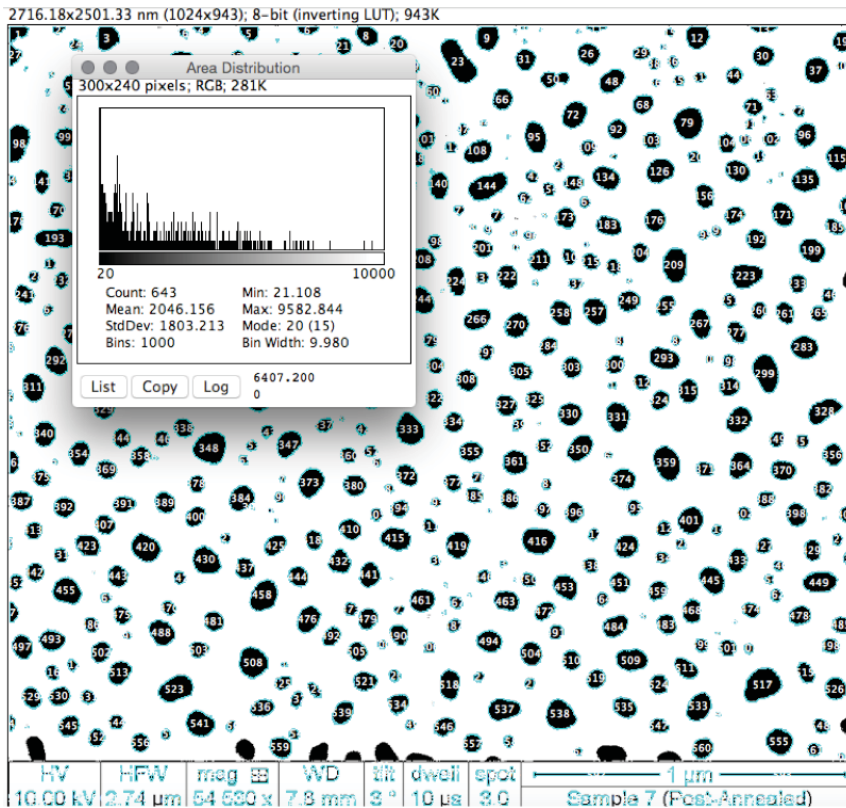
Figure 2.11: Particle area analysis and area distribution histogram

This size distribution allowed for a very thorough comparison between samples grown with different parameters, as well as annealed at different temperatures, granting valuable insight into the exact growth parameters needed to output a given morphology. Furthermore, particle diameter was also calculated from obtained area distribution data, providing side-by-side comparison for both values. Care must be taken in analyzing the diameter curves, however, as eccentricity of a given particle was not made a limiting factor during particle analysis. This inclusion of particles with varying eccentricities can detract from the ability to model particle diameter using the circular area equation, necessitating the need for a side-by-side comparison of both particle area and diameter.

2.2.7 X-Ray Diffraction (XRD). Built around practical application of Bragg's law ($n\lambda=2d\sin\theta$), x-ray diffraction directs an incident supply of x-rays at the sample in question. Figure 2.12 models how these x-rays are then scattered based upon their interaction with the crystallographic hkl planes within the material, and a 2θ vs intensity graph can be generated as these scattered x-rays are collected and detected. This spectra graph provides vital information about the preferred orientations, inter-planar structure, and degeneracy of the material, which allows scientists to make specific, conclusive claims regarding the crystalline structure and phase of a sample.[23]
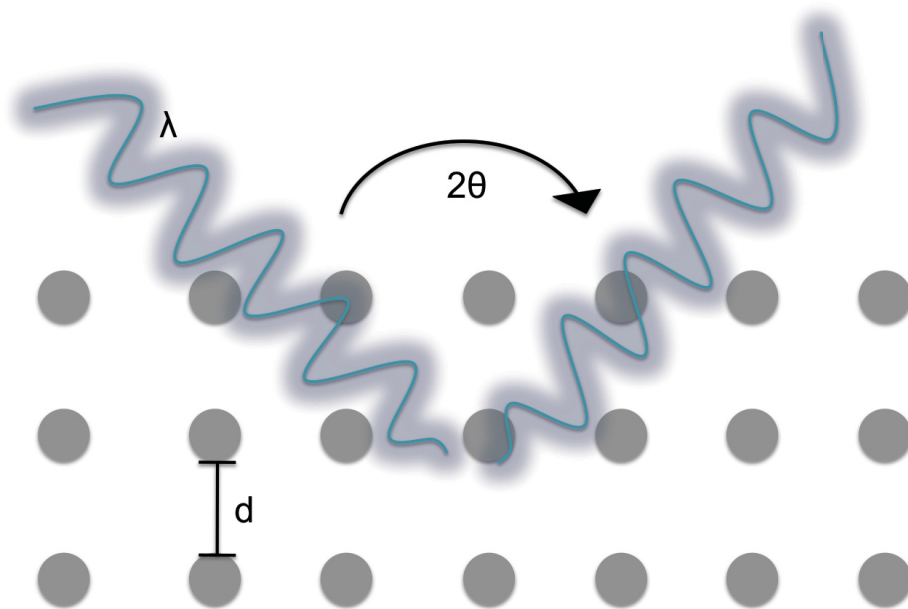
Figure 2.12: X-Ray diffraction dynamics with inter-planar spacing distance d, and incident light of angle θ being diffracted to scatter at 2θ in fulfillment of the Bragg condition

Retrieving the diffraction spectra of a material is only the first step in ensuring valid data collection, however. In order conclusively state the composition of a material based upon x-ray diffraction data, the spectra needs to be verified and checked against

standards on record for that material. This analysis is performed through standard software known was Topas, which allows for a standard spectra to be loaded into the program and checked against experimental data. Furthermore, topas allows for more in depth investigation into active hkl planes and preferred orientations present within the sample. A benchmark for quality of the spectra measured against the standard, known as the goodness of fit, is omnipresent, allowing the user to accept or reject changes based on impact to the goodness of fit. Typical conference and paper submissions require a goodness of fit of roughly 1.4 or less to be accepted.

This thesis study makes use of a Bruker Discover D8 X-Ray Diffractometer, primarily used to take spectra on powders and thin films, to gather data. It is the latter that is of most interest for SERS samples, as the tiny layer of gold nanodots functions as a thin film, introducing several additional complications. While the D8 diffractometer is very capable of mapping the Bragg planes of thin films, special care must be taken to ensure a quality reading. First, the traditional aluminum back plate must be eschewed in favor a glass slide, as the aluminum will provide false peaks for thin film materials, leading to inaccurate data. In addition, the spring located behind the back plate must also be take into account, as this can supply false peaks as well, particularly for samples grown on translucent substrates. Taking this into account, in this study a plastic buffer plate was put into place between the glass back plate and the spring, to somewhat insulate the surface sample from encountering false data. Finally, once the sample is loaded and in place, scans had to be done be done in the x, y, and z directions in order to ascertain the exact position most favorable for a successful scan.

Date taken in this study utilized a locked coupled scan from 10°-80° 2θ, with an

0.2 increment step, and one second taken for each step. Samples 2, 4, 6, and 8 were

scanned in order to analyze the effect of particle morphology and size on x-ray diffraction

spectra. These spectral graphs were taken and analyzed using origin software to

determine peak locations and specifics, modeled in Figure 2.13.

Peak Analysis

Data Set:[Book1]Sheet1!Counts   Date:4/14/2016
Baseline:Line
Chi^2=1.45463E+003 Adj. R-Square=9.83976E-001 # of Data Points=58.
SS=7.70956E+004 Degree of Freedom=53.

Fitting Results

Peak Index	Peak Type	Area Intg	FWHM	Max Height	Center Grvty	Area IntgP
1.	PsdVoigt1	240.84996	0.23578	921.11187	--	100
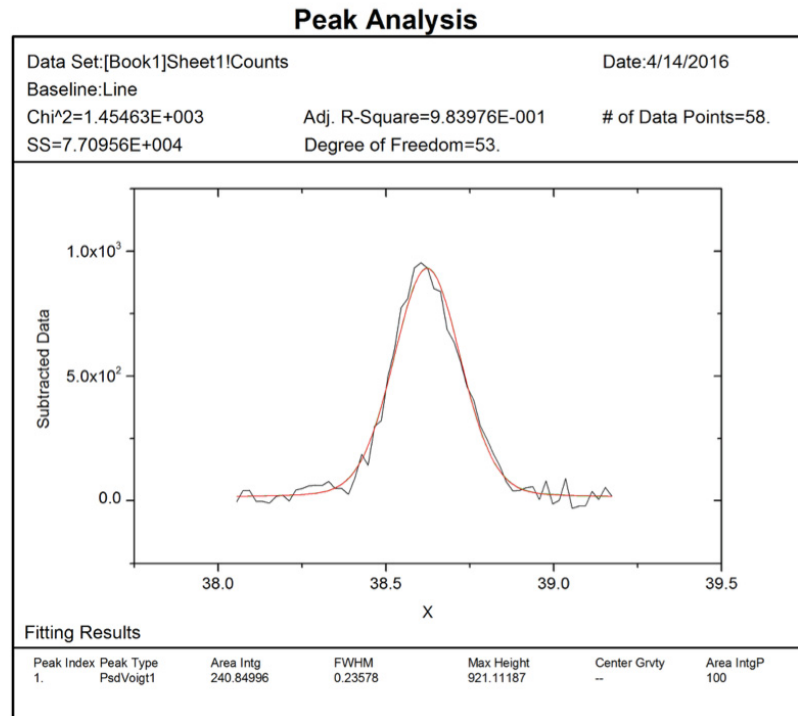
Figure 2.13: Origin peak analysis of 38.5° 2θ peak, determining full-width half-max (FWHM) and peak height

The data was then input into the Scherer equation, shown below, to determine

particle/crystallite size.

$$B = K\lambda/(L\cos(x/2))$$

Where B is the full width half max (FWHM) of the peak, λ is the incident x-ray wavelength, L is the particle diameter, x/2 is the Bragg angle, and K is a numerical constant determined to be roughly .93. There is some inherent assumptions made with the use of this equation, elaborated on in an article by physical review, but it does provide a good approximation of particle size trends to corroborate other analysis methods. [24] It should also be noted that particle size obtained through XRD is typically equal to or smaller than particle size obtained through electron microscopy.[25]

2.2.8 Nanolog Fluoremetry. Characterization by way of fluoremetry is incredibly useful when dealing with optically sensitive materials, and this study ustilized a Horiba styler fluoremeter, shown in Figure 2.14. During a fluoremeter scan, an
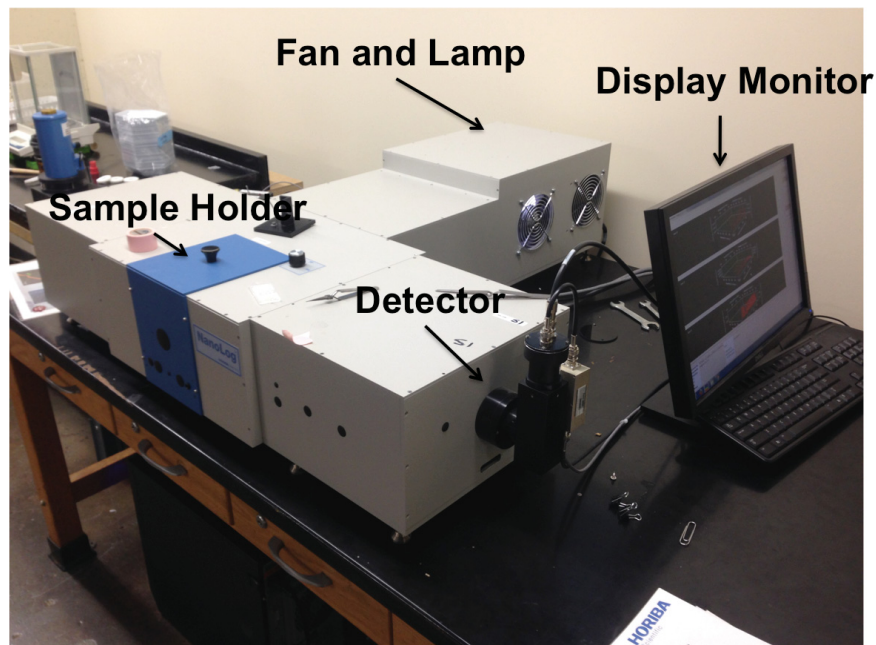
Figure 2.14: Horiba nanolog fluoremeter setup

excitation wavelength of light, or a set of excitation wavelengths, are made incident upon an analyte material. The emission wavelengths are then monitored to characterize the material. If the excitation wavelength possesses the required energy to energize the valance electrons of the material into the conduction band, corresponding emission photon wavelengths will be observed as those electrons fall back into their normal state. This allows for very accurate characterization of semiconductors by way of band gap verification, and has implications for the testing of SERS substrates as well.

Due to the fact that a multitude of excitation wavelengths can be tested with a fluorameter, the localized surface plasmon resonance condition can theoretically be very accurately modeled with this technique. Once the required frequency is met to initialize the plasmon oscillation around the metal nanoparticle, a slight jump in emitted radiation intensity will be observed, manifesting itself as a spike in the data.

Much like Raman spectroscopy, fluorametry suffers from the problems presented by Raleigh scattering, the scattering of photons with the same energy as incident light. As previously discussed, this type of scattering is by far the most prevalent, and thus has the largest intensity count, tending to skew any data around it. Raman spectroscopy has circumvented this problem over time through the use of highly sensitive filters. However, fluoremetry still must contend with this issue, especially in the case of 3D scanning of materials. A full scan with a traditional linear scale will produce a graph that is unintelligible without a large amount of data refinement. This by no means edits out flurometry as a useful characterization technique, but it does introduce some additional steps to gain useful data, and this limitation must be taken into account.

Sample size and placement also proved to be an issue during data collection via fluoremeter measurements. Due to the equipment design and setup of the flourometer used in this study, the space provided for sample placement far out-sizes the sample size itself. This introduced the problem of background contamination within the emission spectra, a problem that has been persistent through all attempts at characterization.

2.2.9 Atomic Force Microscopy. Atomic force microscopy (AFM) presents an incredibly useful supplementary imaging technique that outputs both topographical and phase data for analyte materials. Displayed in Figure 2.15, a spring functionalized cantilever and tip is positioned a set distance away from material, and will attempt to keep this distance constant
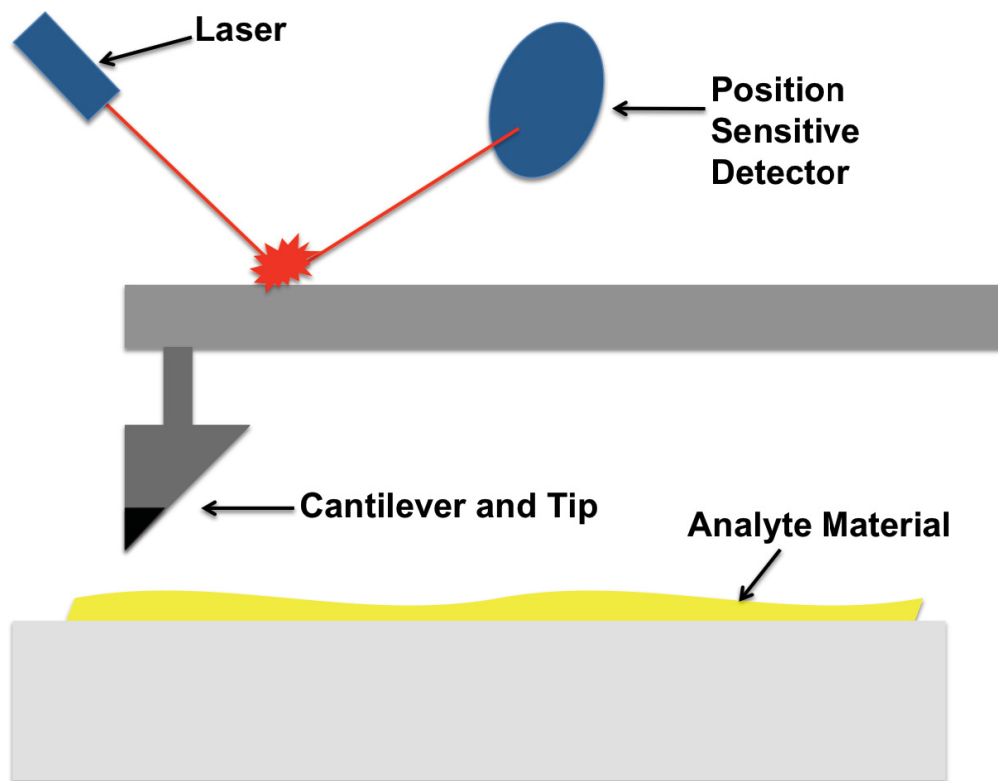
Figure 2.15: Atomic force microscopy dynamics

throughout data collection. This constant distance represents a key factor in the techniques viability, as it allows for height differential of the sample to be characterized without actual contact and potential damage of the sample. This height change is calculated through the introduction of an incident laser on top of the cantilever setup, and the reflection of that light off a mirror and into a position sensitive detector. As the cantilever moves up and down, the light will reflect and reach the detector at different angles, allowing for height to be determined. This results in a highly accurate topographical map of the substrate being produced.[26]

One important benefit of the characterization tool to this thesis revolves around the purely physical nature of the data collection. In direct contrast with scanning electron microscopy, which requires a conductive substrate to be able to image with a high degree of accuracy, atomic force microscopy can function on any type of substrate, provided it is relatively flat. This presents a unique opportunity for the direct imaging of insulating SERS substrates, something previously incredibly difficult due to the necessity of an insulating substrate in their function. The mechanical phase composition of the constituent material can also be mapped to a reasonable degree of accuracy through utilizing a tapping scan mode. With this method, the cantilever tip will tap the material at high at high speeds, producing different vibration based on the mechanical properties of the substance. Analysis of this difference can help to determine the boundaries of the constituent materials

To take images, samples were placed on the tray pictured in Figure 2.16, and the silicon tipped cantilever was lowered to begin data collection. The cantilever was traced along the sample in a tapping mode line scan, and retraced to ensure image accuracy.
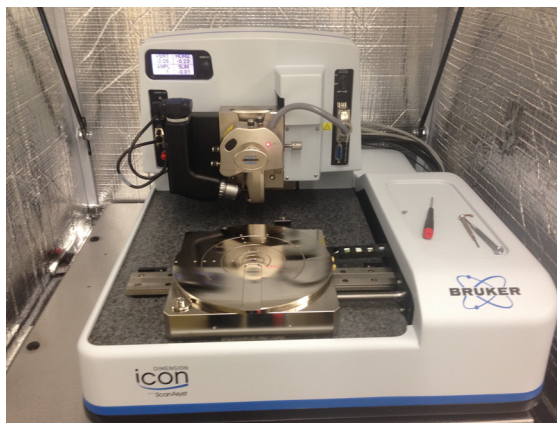
Figure 2.16: Atomic force microscope located in the Jordan Valley Innovation Center

An additional benefit of highly sensitive topographical mapping software is the ability to output data for the surface roughness of a given area. By restricting the height measurement distribution area to a single nanoparticle, the distribution curve will reflect strictly the properties of that nano-particle, allowing for its particular roughness to be calculated.[27]

Image J AFM image analysis was also performed on the topographical AFM images, calculating both particle size and particle-to-particle distance distribution curves. Analysis and calculations were performed in a manner analogous to SEM image analysis.

2.2.10 Raman Spectroscopy. Previously discussed within the introduction section, Raman spectroscopy is the practice of making a laser of a specific wavelength incident upon a material, and monitoring the photons ejected from the analyte to determine internal phonon dynamics. This allows for extensive characterization of materials, resulting in the production of stock spectras that can be individually mapped to very specific substances. This individualization and specificity is what makes Raman a premier characterization tool in the science community.

In this study, the dye rhodamine-6G (R-6G) was utilized in order to test for Raman excitation ratios within the different samples. R-6G was chosen due to its strong Raman spectra and prevalence within the literature, proving it as a strong candidate for SERS confirmation.[28-29] R-6G was dispersed within DI water to a concentration of .24286 g/L, or $5.062 * 10^{-4}$ M, and drop-casted on both untreated quartz and the synthesized substrates. The substrates were then analyzed with a 532 nm laser and data was collected with a D1 filter and a 200 μm hole size.

Samples were formatted and analyzed using Origin software, and the scattering enhancement factor was determined using the analytical enhancement factor equation, shown below:

$$\text{Analytical Enhancement Factor (AEF)} = (I_{SERS}/C_{SERS}) / (I_{RS}/C_{RS})$$

Where I is intensity and C is concentration.[30] Due to the fact that the same concentration, .24286 g/L, was used both with and without SERS, the AEF equation simplifies down to:

$$\text{Analytical Enhancement Factor (AEF)} = (I_{SERS}/I_{RS})$$

which provides the enhancements factors shown in the results section.

CHAPTER 3: RESULTS AND DISCUSSION

3.1 Scanning Electron Microscopy (SEM)

Scanning electron microscopy, despite being a purely visual form of material characterization, offers some insight into several different areas of nanoparticle synthesis. First, as can be seen from Figure 3.1-3.4 below, thickness and amount of initial gold film coating will play a key role in annealment dynamics, and ultimately particle morphology. Increasing sputter time and amperage will both increase the amount of gold deposited on the substrate, with the increase from 10-20 mA causing the largest jump in film thickness. This thickness change is especially apparent when one compares Figure 3.2 (a) and Figure 3.4 (a), both samples being identical save for an amperage shift. With each increase in amount of film coverage, there is a corresponding jump in particle order, size, and even uniformity displayed after annealing treatments, suggesting a slow trend toward bulk behavior. This can be explained by the amount of initial gold available for relocation during annealing of the sample. In earlier samples with a lower amount of deposited gold, many different nucleation sites begin to form, as there is a somewhat incomplete coating on the surface. In contrast, the heavier coatings have more material to agglomerate, and thus form larger structures more readily.

In regards to annealment temperature, it seems clear that with the increased energy supplied by the 500°C ambient temperature, more uniform, circular structures began to form. This could indicate melting dynamics at play, with surface tensions pulling outermost atoms back into the nucleation site.
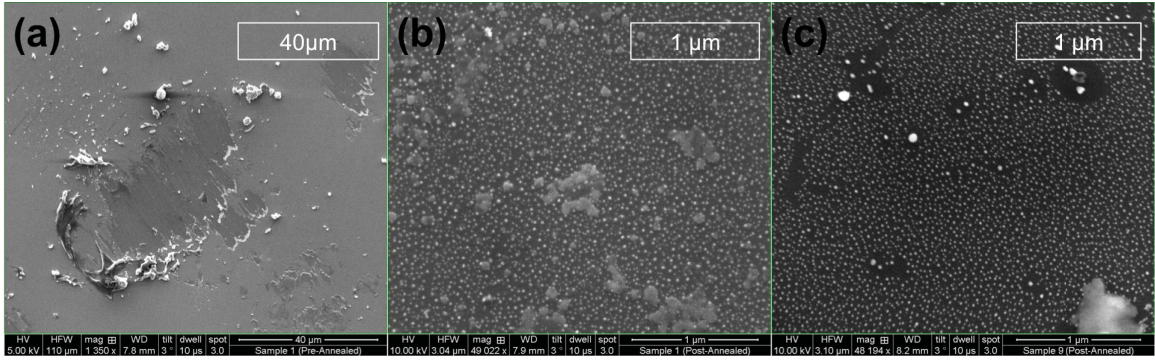
Figure 3.1: Gold sputtered on silicon for 20 seconds with a 10 mA current (a) directly after sputtering, (b) after a one hour 300°C anneal, and (c) after a one hour 500°C anneal
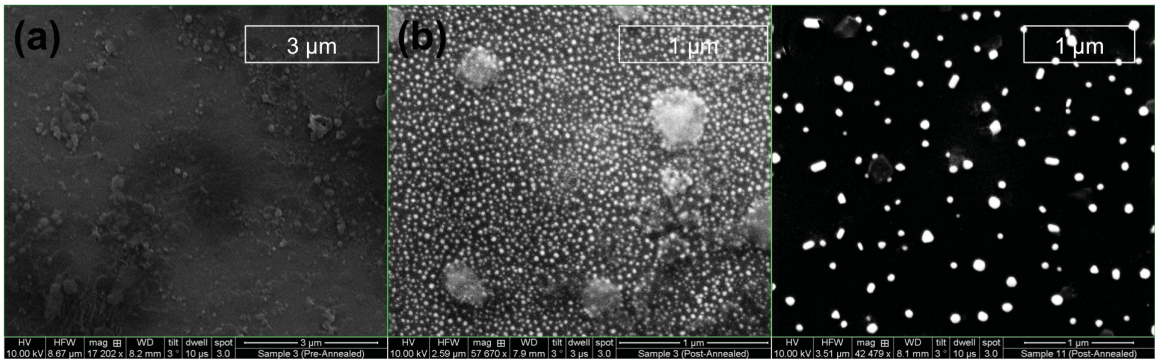
Figure 3.2: Gold sputtered on silicon for 40 seconds with a 10 mA current (a) directly after sputtering, (b) after a one hour 300°C anneal, and (c) after a one hour 500°C anneal.
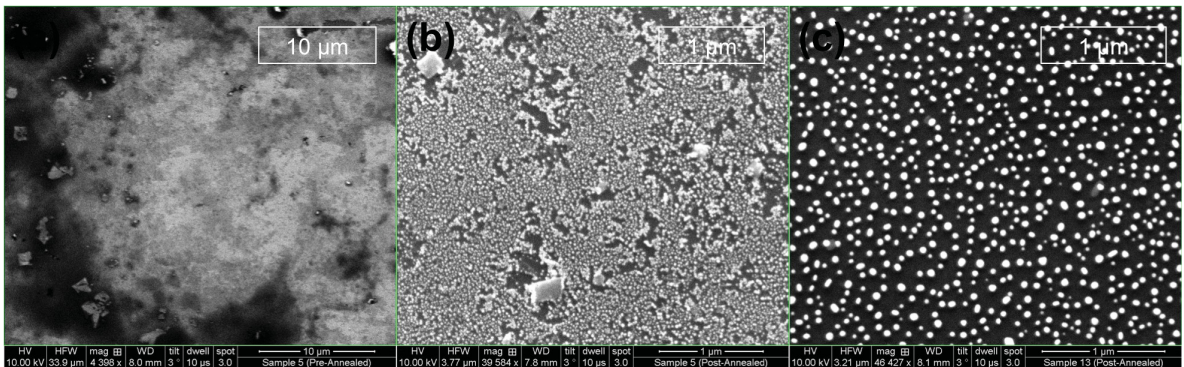
Figure 3.3: Gold sputtered on silicon for 20 seconds with a 20 mA current (a) directly after sputtering, (b) after a one hour 300°C anneal, and (c) after a one hour 500°C anneal.
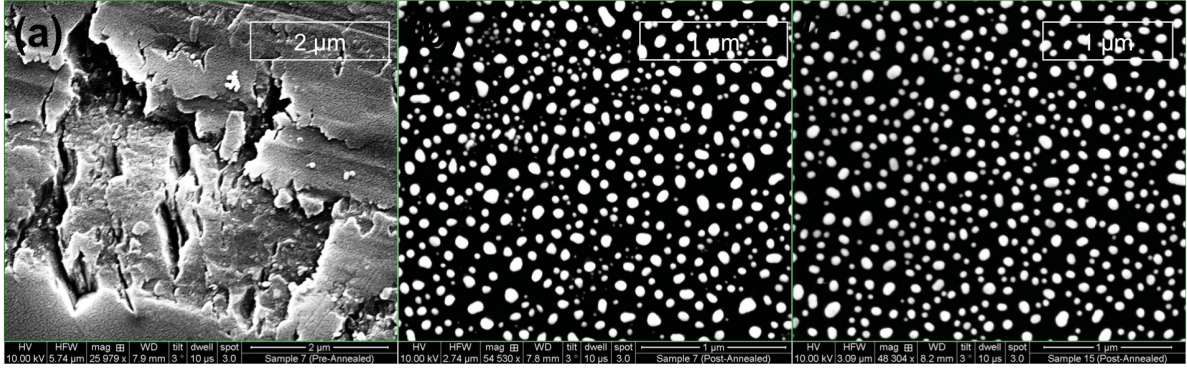
Figure 3.4: Gold sputtered on silicon for 40 seconds with a 20 mA current (a) directly after sputtering, (b) after a one hour 300°C anneal, and (c) after a one hour 500°C anneal.

There is also evidence for increased sublimation of material, as there seems to be less material deposited between nucleation sites during the 500°C annealment treatment. This change could potentially be due to increase melting of surface material, but the absence could also be due to a direct sublimation into the environment.

Finally, and perhaps most commercially important, each microscopy photo has a one μm scale bar, displaying the large area of relatively uniform coverage provided through this technique. This displays the scalability of this technique, as the area patterned by the gold nanodots seems only to be limited by the sputter chamber used in the deposition.

3.2 SEM Image Analysis

Through analysis of the data obtained from Image J analysis software, distribution curves and histogram data could be calculated for both particle area and particle-to-particle distance.

Compiled within Figure 3.5, the particle area and diameter of the sample set annealed at 300°C display a much stronger prevalence toward smaller particle sizes, primarily around 5-10 nm.

300°C Anneal Particle Area Distribution

(a)

300°C Anneal Particle Diameter Distribution
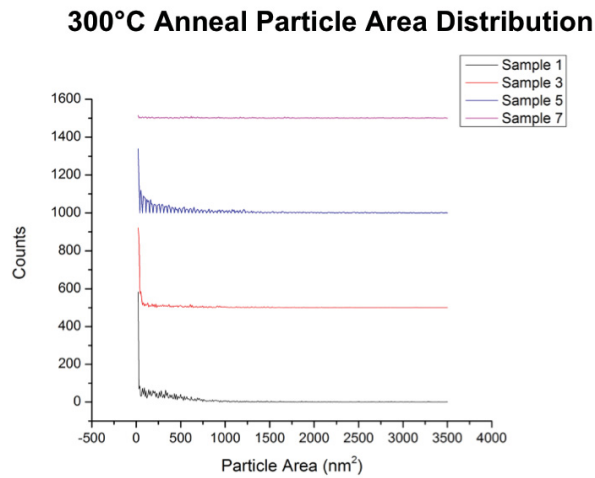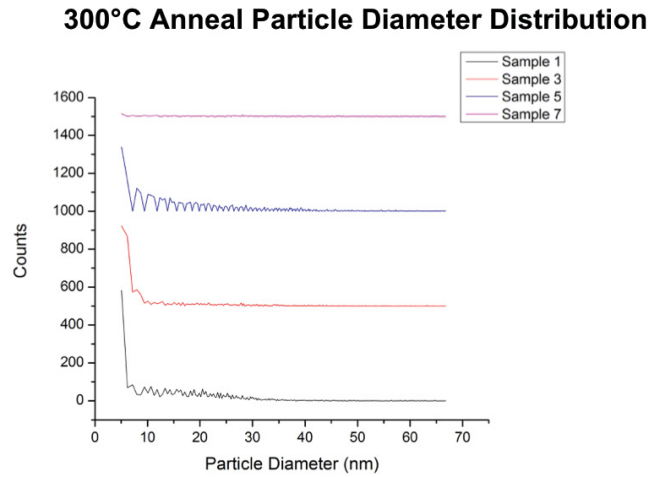
(b)

Figure 3.5: (a) Particle area and (b) particle diameter comparison of samples 1, 3, 5, and 7. All annealed at 300°C for one hour.

This indicates a lack of mobility of the surface hold atoms on the substrate. The thermal energy provided by the annealment temperature has not yet reached the necessary critical point to allow for true agglomeration sites to form and construct larger structures, halting the process of thin film synthesis before a continuous structure can be formed. There is an aberration in this trend with sample 7, as it displays distribution set more in line with samples annealed at higher temperatures, a distribution more skewed toward a larger particle size. This can be explained by the increased abundance of gold available from an increased film thickness. Though atomic migration is limited due to the lack of thermal excitation, each atom has a decreased mean free path, allowing for larger structures to form with less energy provided.

Analysis of the sample set annealed at 500°C has been broken into two parts, Figure 3.6 and Figure 3.7, due to large difference between sample 9 and the others within the set.

Much like sample 7 of the previous set, sample 9 displays a trend more in line with a different annealment temperature. This discrepancy is also due the amount of gold deposited; sample 9 simply does not have the raw material required to bring its atomic sites together into larger area of agglomeration, resulting in more numerous, smaller agglomeration sites. Samples 11, 13, and 15, do display the increase in particle size that one would expect to come with a higher temperature, further cementing the conclusions drawn from the SEM images analyzed previously.

Sample 9 Particle Area Distribution

(a)

Sample 9 Particle Diameter Distribution
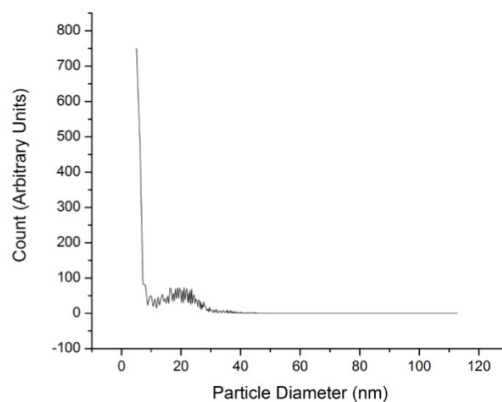
(b)

Figure 3.6: (a) Particle area and (b) particle diameter of sample 9. Annealed at 500°C for one hour

For the samples annealed at 300° C, particle distance seems to follow a fairly linear trend, with particle to particle distance increasing as thickness of deposited gold coating increases. This is an interesting result, as traditional logic would dictate with less material to work with, the distance between nucleation sites would be greater. However, when one takes into account the vast discrepancy in number of particles between sample

44

1 and sample 7, displayed in Figure 3.8, this dynamic begins to make more sense. With a thinner coating, many smaller particles are formed, with smaller distances between each individual particle. In contrast, a thicker layer gives rise to a smaller number of larger particles, and a somewhat larger area in between.
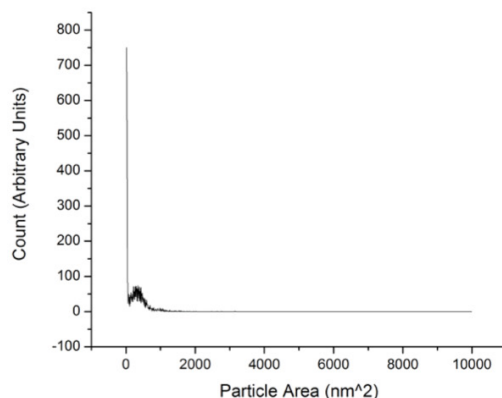

(a)
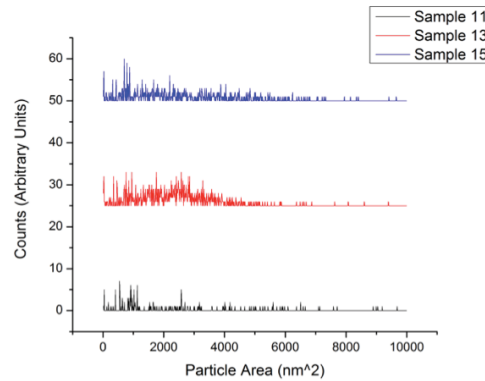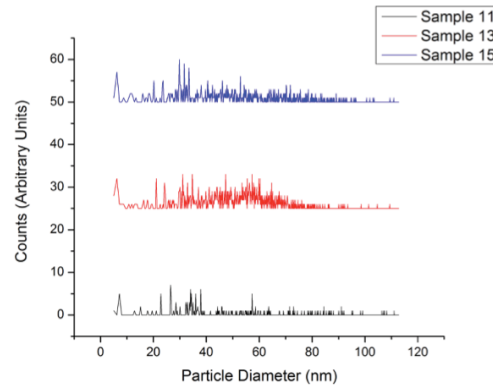
(b)

Figure 3.7: (a) Particle area and (b) particle diameter comparison of samples 11, 13, and 15. All annealed at 500°C for one hour.

Particle to particle distance analysis on samples annealed under 500°C show the same dynamics as those annealed at 300°C, with one notable exception. Sample 11, modeled in F 3.9 (b), clearly deviates from the traditional trend established by all other sample sets. This deviance from the norm could be attributed to the central nature this particular sample has when compared to the others. Sample 11, sputter deposited at 10 mA for 40 seconds, resides at a point directly in between the smaller size, smaller interparticle distance model of samples with thinner films, and the larger mold cast by thicker film samples. The initially chaotic data set shown by F 3.9 (b) could therefore display the transition between these two modes. The sample begins to have enough thermal energy to allow for more widespread atomic movement, but not enough material to support the larger number of agglomeration sites shown in later samples.
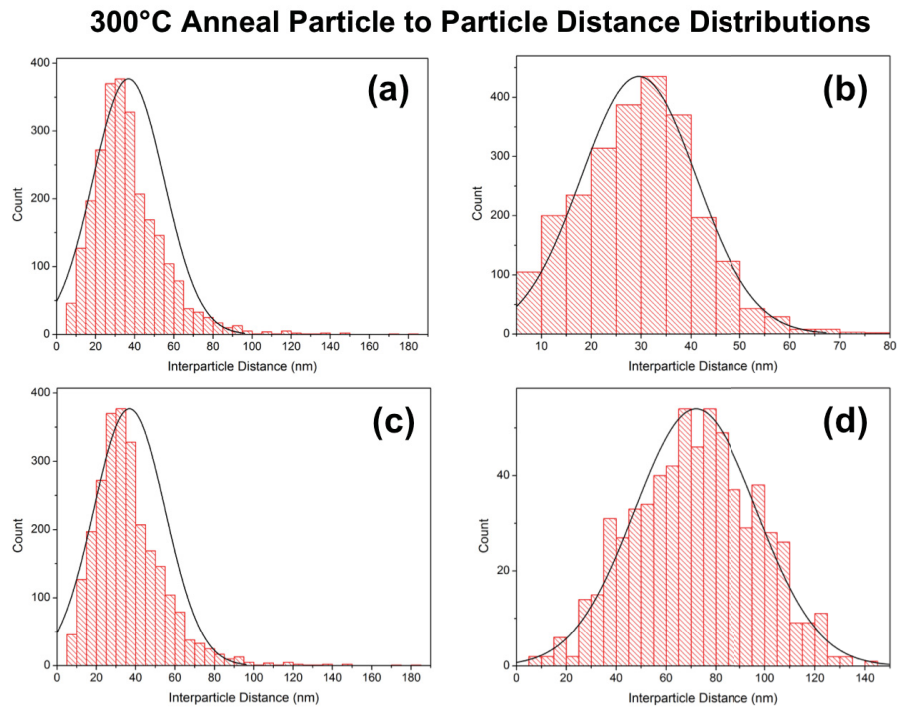
Figure 3.8: Particle to particle distance graphs for (a) sample 1, (b) sample 3, (c) sample 5, and (d) sample 7. All annealed at 300°C

500°C Anneal Particle to Particle Distance Distributions
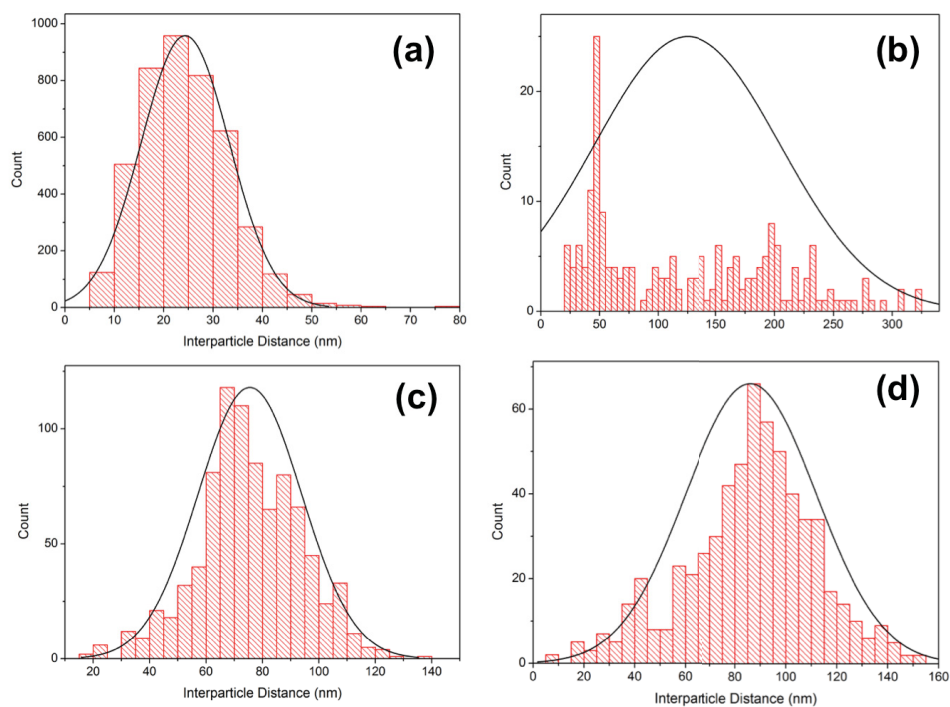
Figure 3.9: Particle to particle distance graphs for (a) sample 9, (b) sample 11, (c) sample 13, and (d) sample 15. All annealed at 500°C

3.3 X-Ray Diffraction (XRD)

Samples 2, 4, 6, and 8 were scanned in order to gauge the effect of particle morphology on x-ray diffraction peaks. Sample 2 unfortunately produced a coating too thin to be imaged with any reliability, but samples 4. 6, and 8 exhibited the traditional {1 0 0} gold peak seen at roughly 38.5 2θ. These results are summarized below in Figure 3.10. The fact that the {1 0 0} peak is by far the most prevalent within the data suggest sublimation may indeed be occurring during the annealing process. Literature suggests the {1 0 0} plane to be one of the most energetically favorable, and typically occurs post sublimation for noble metals.

300°C Anneal XRD Comparison
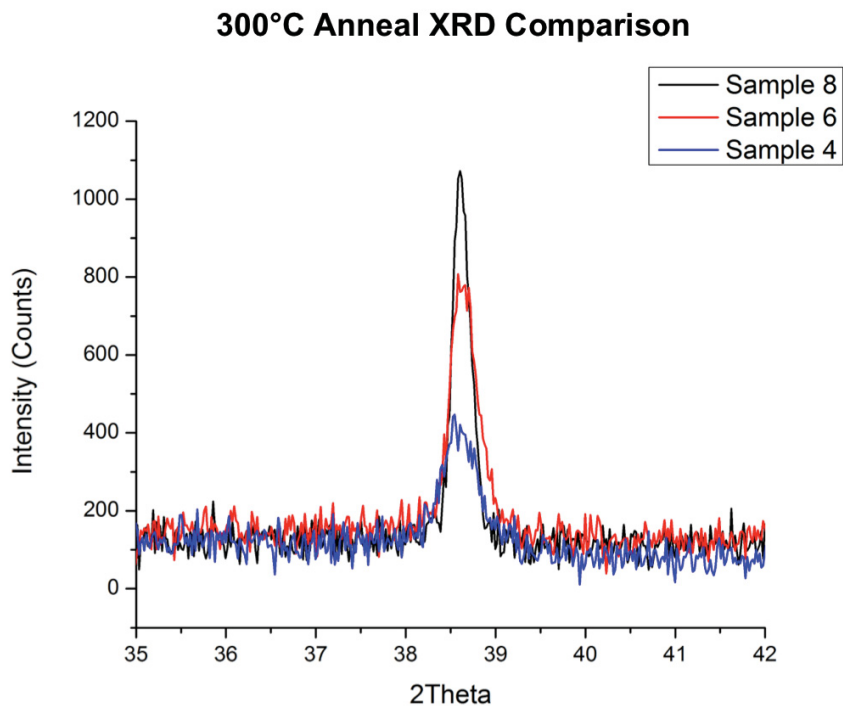
Figure 3.10: X-ray diffraction spectra of samples 4, 6, and 8, all annealed at 300°C for one hour and displaying the characteristic [1 0 0] peak at 38.5° 2θ

A gradual broadening of the {1 0 0 } peak can be detected between samples 8, 6, and 2. This can be attributed to s decrease in particle, size, which was calculated using Scherrer's equation.

Table 3.1: Scherrer particle size analysis of samples annealed at 300°C for one hour XRD peaks

Sample Number	FWHM	2θ	Linear Crystallite Size
8	0.236	38.604	6.8
6	0.351	38.663	4.6
4	0.469	38.604	3.4

3.4 Atomic Force Microscopy (AFM)

3.4.1 300°C Annealment Comparison. Within the sample set annealed at 300°C, there is a clear pull toward larger particle size with an increased initial film thickness, supporting and complementing the data obtained through SEM analysis as well as confirming somewhat similar growth dynamics on the silicon substrate used for the electron imaging and the quartz used for the atomic force imaging. This is an important distinction, as SERS must occur on an insulating substrate, so it is integral to sample analysis that conclusion can be drawn from imaging gold deposited on conductive substrates, as is dictated by the requirements of scanning electron microscopy.

Within the phase dependent images, shown on the right of Figure 3.11-3.14, the already exhibited trend toward larger particle size with increased film thickness is supported. The topographical maps located on the left demonstrate a somewhat even height measurement within the each individual nanoparticle. This indicates a somewhat smoother particle, which will be elaborated on further in a later section.

Figure 3.11 AFM images of (a) sample topography (2D and 3D) and (b) phase of sample 2, gold deposited at 10 mA for 20 seconds and annealed at 300°C for one hour
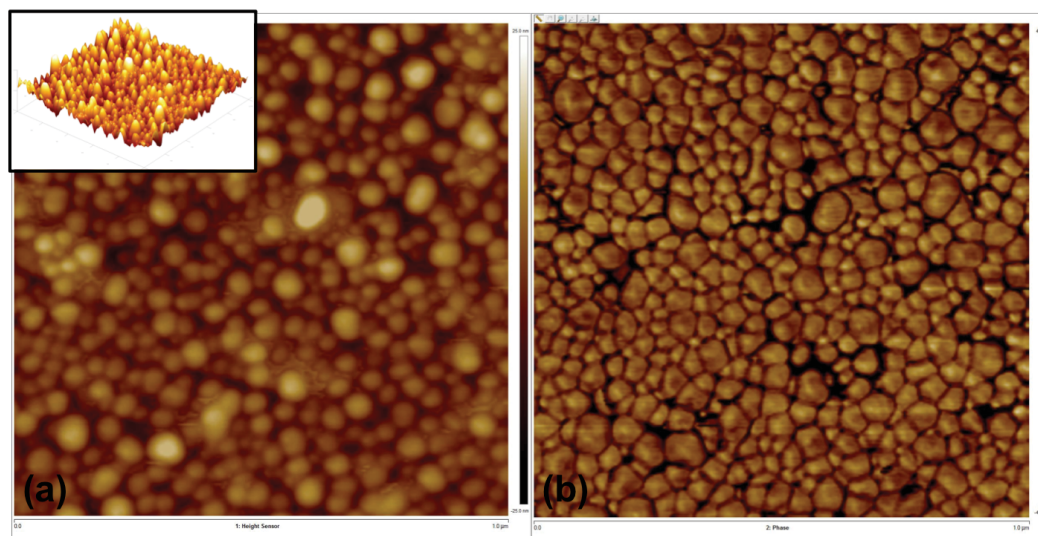
Figure 3.12 AFM images of (a) sample topography (2D and 3D) and (b) phase of sample 4, gold deposited at 10 mA for 40 seconds and annealed at 300°C for one hour
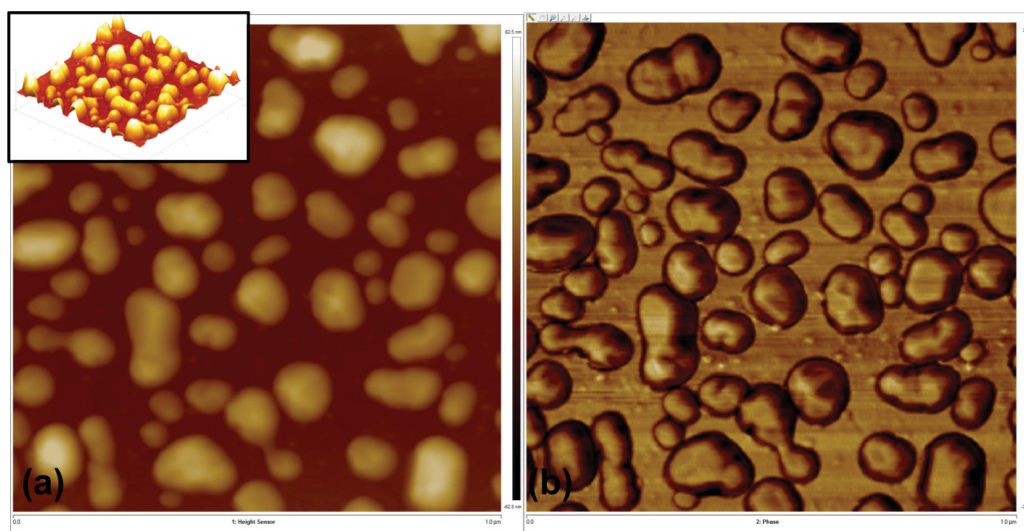
Figure 3.13 AFM Images of (a) sample topography (2D and 3D) and (b) phase of sample 6, gold deposited at 20 mA for 20 seconds and annealed at 300°C for one hour
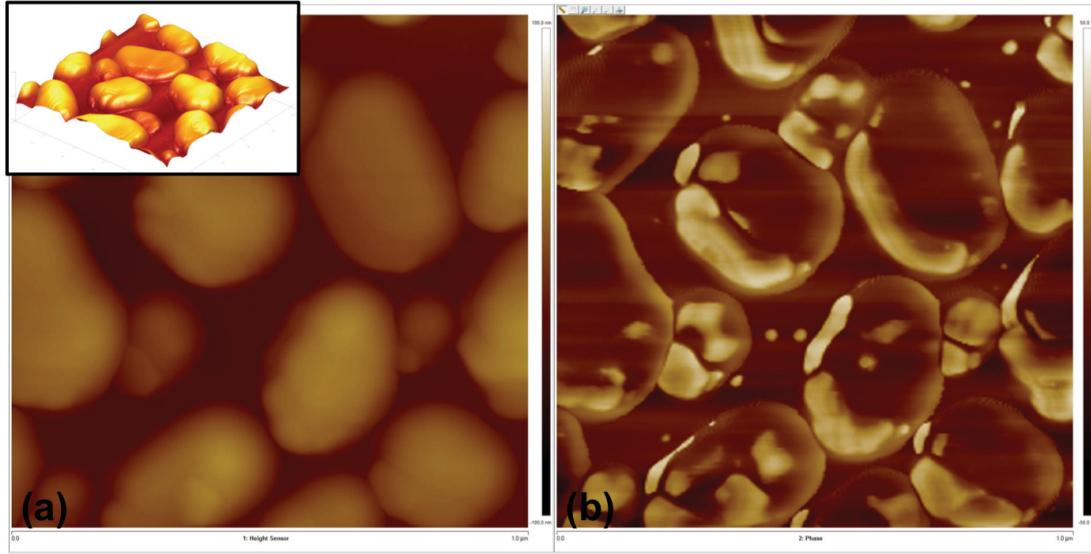
Figure 3.14 AFM Images of (a) sample topography (2D and 3D) and (b) phase of sample 8, gold deposited at 20 mA for 40 seconds and annealed at 300°C for one hour

3.4.2 500°C Annealment Comparison. The following samples, shown in Figure 3.15-3.18, were annealed at 500°C for one hour.
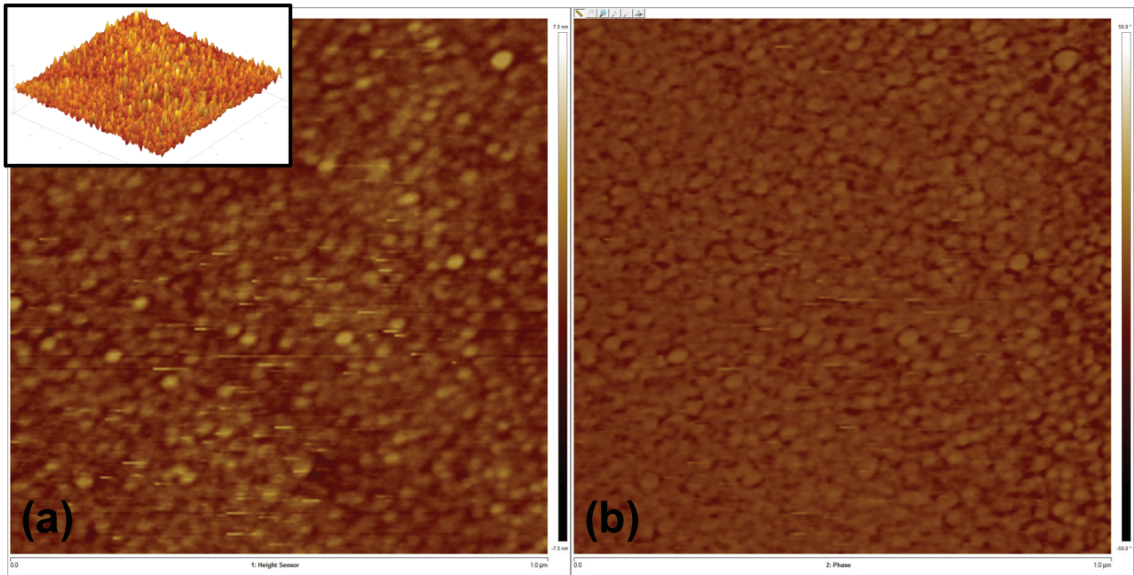
Figure 3.15 AFM Images of (a) sample topography (2D and 3D) and (b) phase of sample 10, gold deposited at 10 mA for 20 seconds and annealed at 500°C for one hour
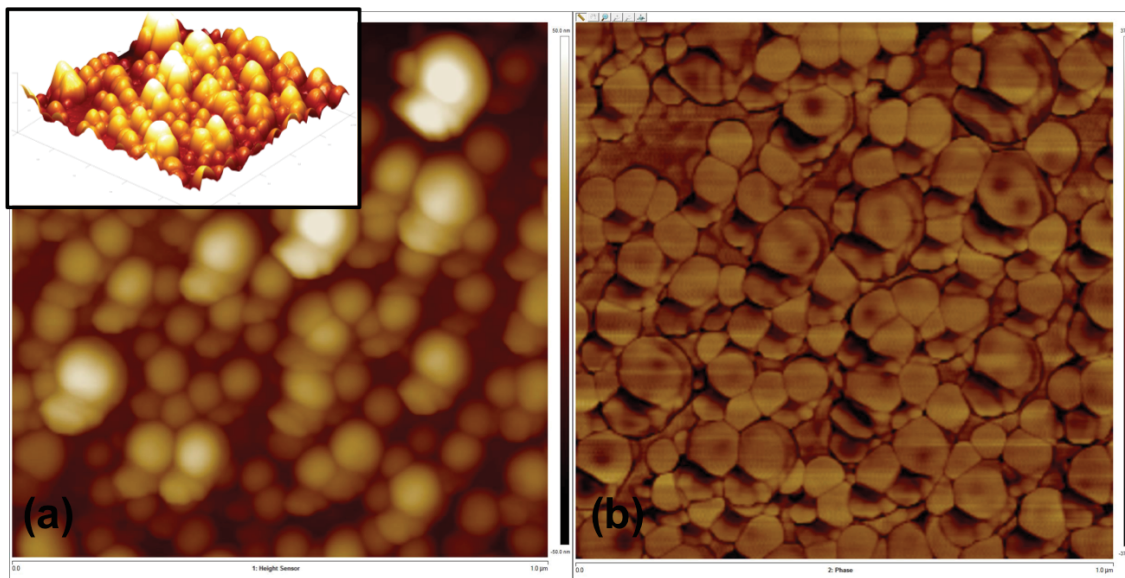
Figure 3.16 AFM images of (a) sample topography (2D and 3D) and (b) phase of sample 12, gold deposited at 10 mA for 40 seconds and annealed at 500°C for one hour
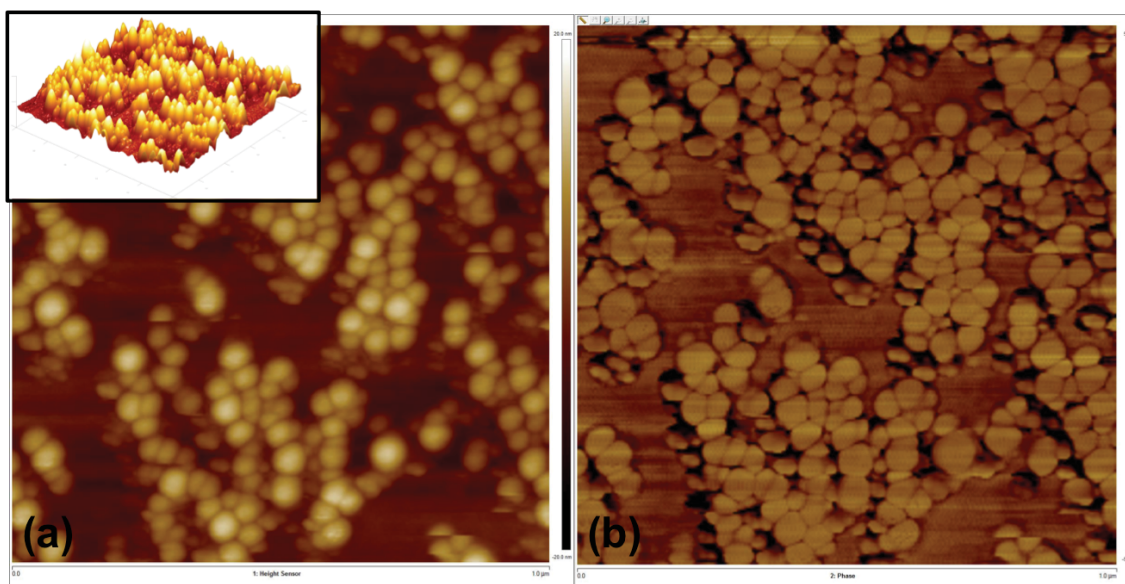
Figure 3.17 AFM images of (a) sample topography (2D and 3D) and (b) phase of sample 14, gold deposited at 20 mA for 20 seconds and annealed at 500°C for one hour
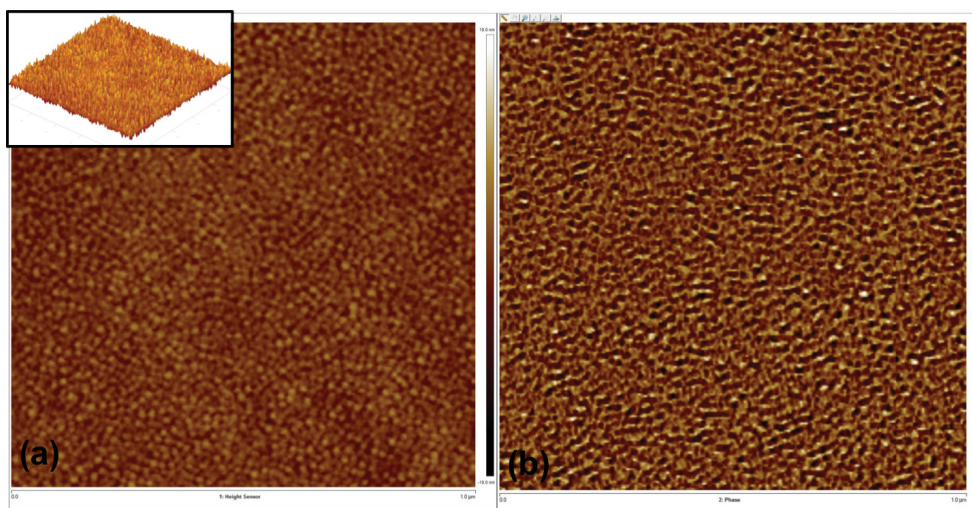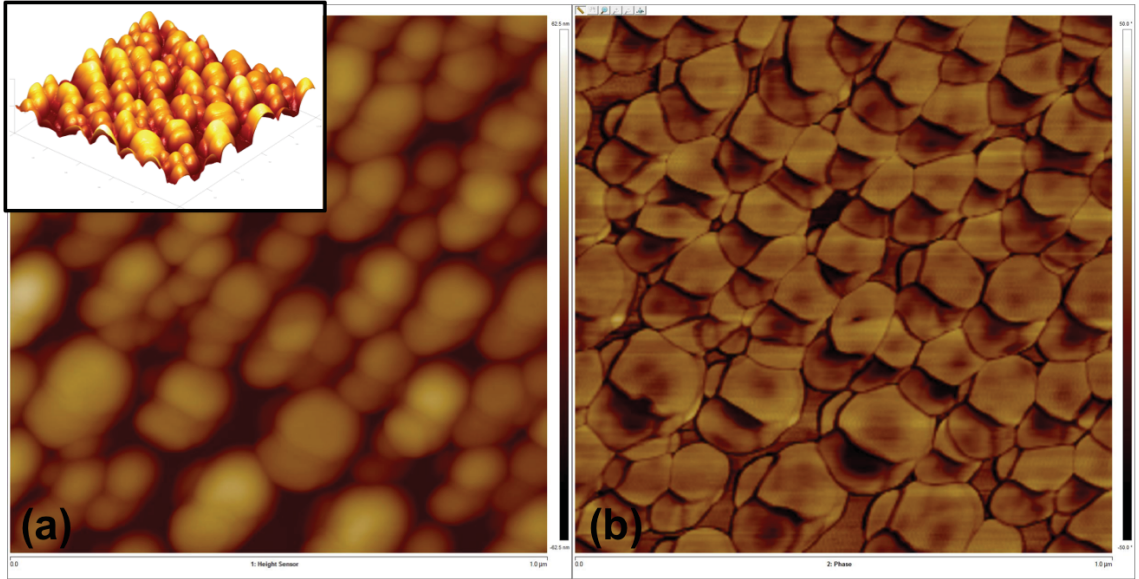
Figure 3.18 AFM Images of (a) sample topography (2D and 3D) and (b) phase of sample 16, gold deposited at 20 mA for 40 seconds and annealed at 500°C for one hour

AFM images of samples annealed at 500°C begin to present a problem for topographical as well as phase diagram accuracy, and therefore observers must be cautious to take special note of the 3-dimensional topographical plot when making conclusions about the data. This is potentially due to increased amount of gold present on the substrate, which will interfere with any kind of phase reading. With that in mind, Figure 3.15-Figure 3.18 also corroborate data obtained through scanning microscopy, with larger structures being formed in samples 11, 13, and 15, and sample 9 retaining a smaller particle size. Sample 11, the aberration discussed in the previous imaging section, seems to once again occupy the middle ground, with larger particles beginning to form together, but with vey large spaces in between.

3.4.3 Height Distribution and Surface Roughness. When discussing particle height data obtained through atomic force microscopy, care must be taken to interpret results correctly. Unlike the image analysis data obtained from scanning electron

microscopy images, these values are not restricted to the particles themselves,

incorporating substrate height into the data curve as well. However, if one is logical in

looking at the data curve, this does not present an insurmountable barrier to obtaining a

true height average for the nanoparticles present on the surface.

Within the samples annealed at 300°C, there is a fairly predictable pattern that

begins to emerge in Figure 3.19 as initial film thickness begins to rise.

300°C Anneal Particle Height Distribution
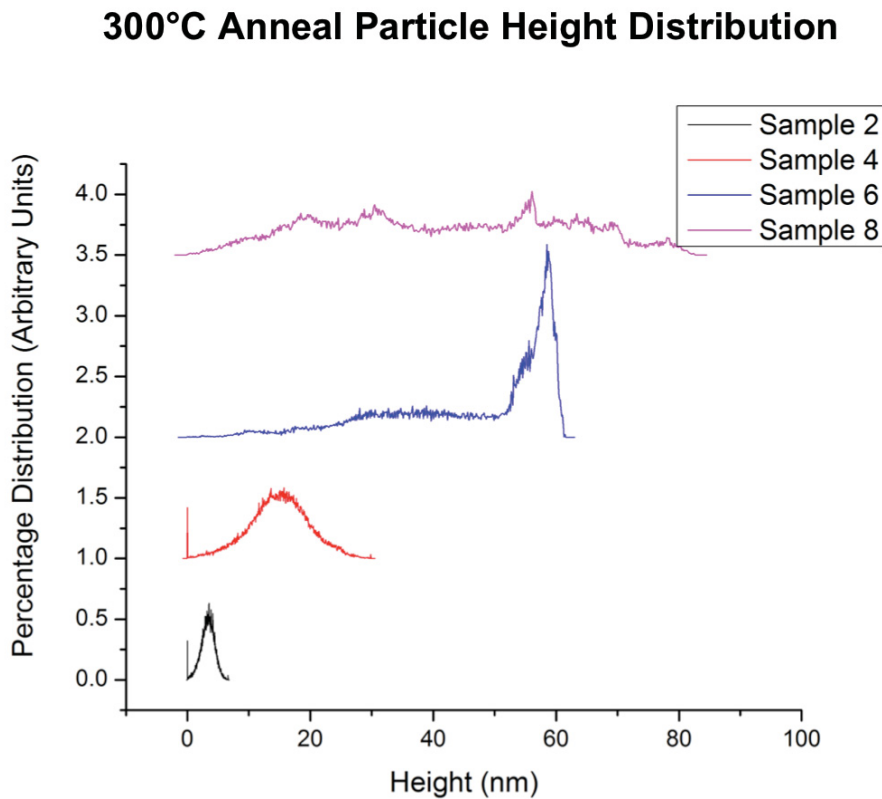
Figure 3.19: Particle height distribution of samples 2, 4, 6, and 8. All annealed at 300°C
for one hour.

As previously mentioned, the substrates height measurements are included on

these data curves. Nonetheless, the sharper spikes in height percentage distribution take

place toward the larger height values, something that would be impossible for the

substrate to contribute to. This suggests that the deposited nanoparticle occupy a large section of the surface as well as certifying that it is indeed the nanoparticles of interest that make up this part of the data curve. With that in mind, it can be seen that as sputter time and amperage are increased, particle height also increases, to a point. Sample 8, the thickest in this sample set, begins to display more of a distribution of sizes, as opposed to the sharp spikes seen in samples 2, 4, and 6. This suggests that the initial coating was thick enough to trend the material more toward a bulk arrangement.

Samples annealed at 500°C display the same general trend in height distribution the previous sample set exhibited. Within Figure 2.20, a stronger preference for a specific particle height is displayed by samples with a smaller amount of initial gold deposited, and those with thicker initial coatings having more of a uniform distribution of height.

Sample 14 presents an interesting case when contrasted with sample 6 of the previous set. Both were deposited at 20 mA for 20 seconds, with the only difference in their synthesis method being the annealment temperature. Sample 6, with less energy being provided by its 300°C anneal temperature, did not have the necessary freedom in atomic movement to form larger structures, restricting it to a larger number of similarly sized smaller nucleation sites.

Also worthy of mention is the orientation of the formed nanostructures with respect to the substrate. In many of the three-dimensional plots pictured above, the nanostructures are orientated reasonably close to a 90° angle with the surface, indicating at least some preference toward growth in the z direction.

500°C Anneal Particle Height Distribution
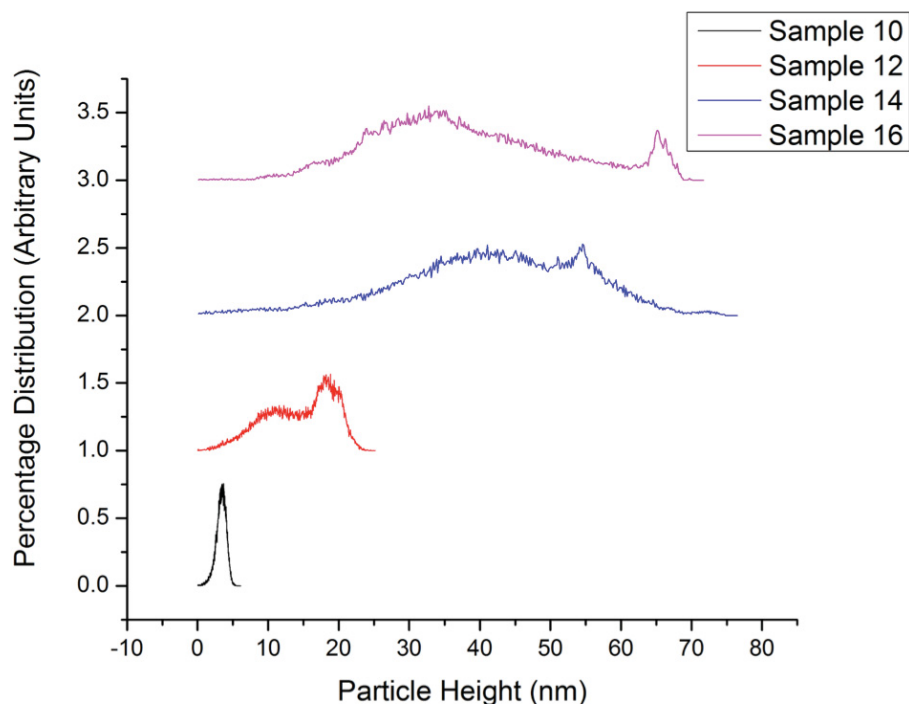
Figure 3.20: Particle height distribution of samples 10, 12, 14, and 16. All annealed at 500°C for one hour.

Furthermore, the difference displayed in particle height distribution between anneal temperatures can provide additional details regarding the melting and sublimation of gold particles during furnace treatments. Within the samples 14 and 16, there is a much larger tendency toward smaller particle height than in corresponding samples within the 300°C anneal sample set. As AFM height results are not taken from a particle-to-particle basis, but point-to-point, this height discrepancy can indicate an overall loss of gold during the higher temperature furnace treatment. As this can only occur through loss of gold to air, sublimation must be occurring.

3.5 AFM Image Analysis (Image J)

Samples annealed at 300°C display the same general trend exhibited within the SEM image analysis, with a few discrepancies. Most prevalent among them is the tendency of gold on quartz to form larger structures more quickly, as can be seen in the more uniform distributions of samples 4, 6, and 8 in both particle area and diameter displayed in Figure 3.21.

300°C Anneal Particle Area Distribution

(a)
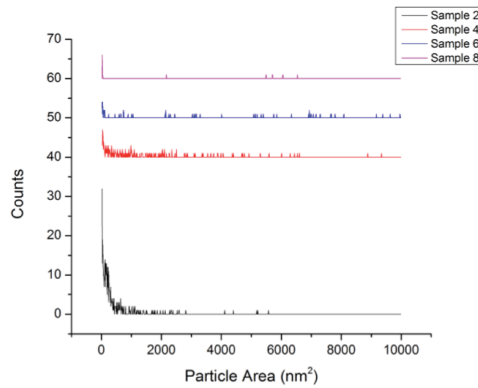
300°C Anneal Particle Diameter Distribution
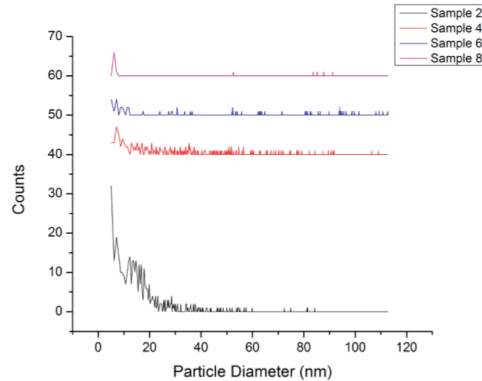
(b)

3.21: (a) Particle area and (b) particle diameter comparison of samples 2, 4, 6, and 8. All annealed at 300°C for one hour.

Seen below in Figure 3.22, the 500°C sample set follows the trends exhibited by the other samples very smoothly. Smaller particles size being more prevalent in the thinner film, and more agglomeration exhibited in the other samples.

500°C Anneal Particle Area Distribution
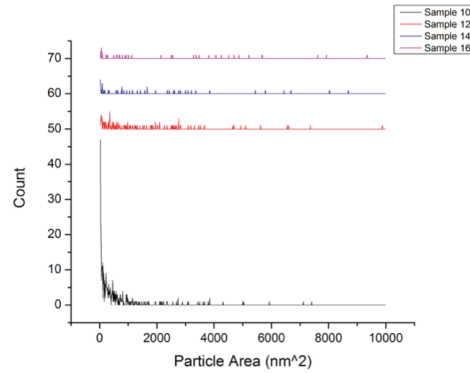
(a)

500°C Anneal Particle Diameter Distribution
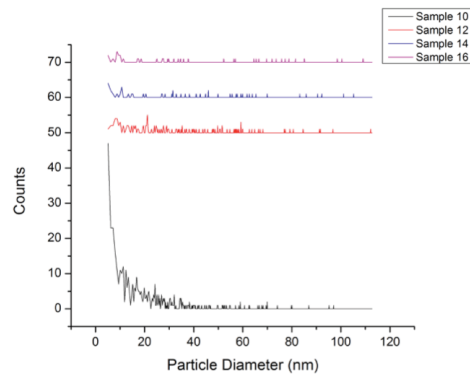
(b)

Figure 3.22: (a) Particle area and (b) particle diameter comparison of samples 10, 12, 14, and 16. All annealed at 500°C for one hour.

Particle to particle distance shows more interpretable trends when particles are more easily distinguished from each other, with a typical Gaussian curve being unable to

capture the trends exhibited by substrate that display more particle agglomeration, as can be seen from the more random distribution seen within Figure 3.23 (c) –(d) and Figure 3.24 (c). In general these results tend to support those found with silicon substrates, with larger particles producing larger particle-to-particle distances.

300°C Anneal Particle to Particle Distance Distributions
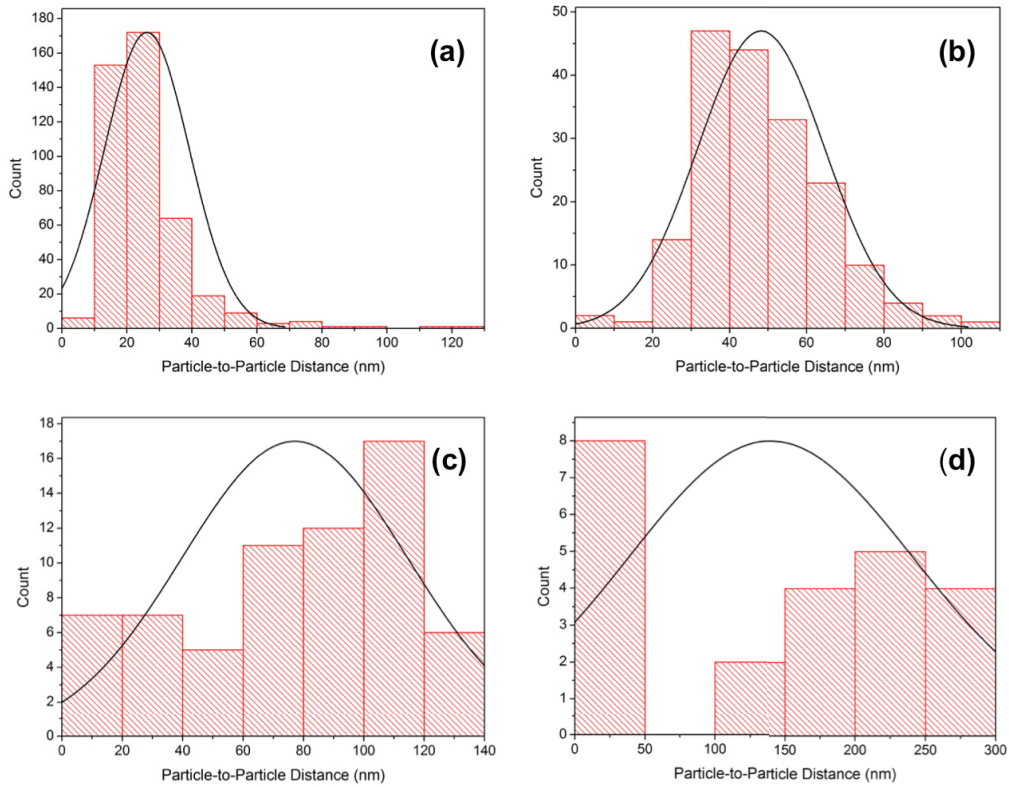
Figure 3.23: Particle to particle distance graphs for (a) sample 2, (b) sample 4, (c) sample 6, and (d) sample 8. All annealed at 300°C

500°C Anneal Particle to Particle Distance Distributions
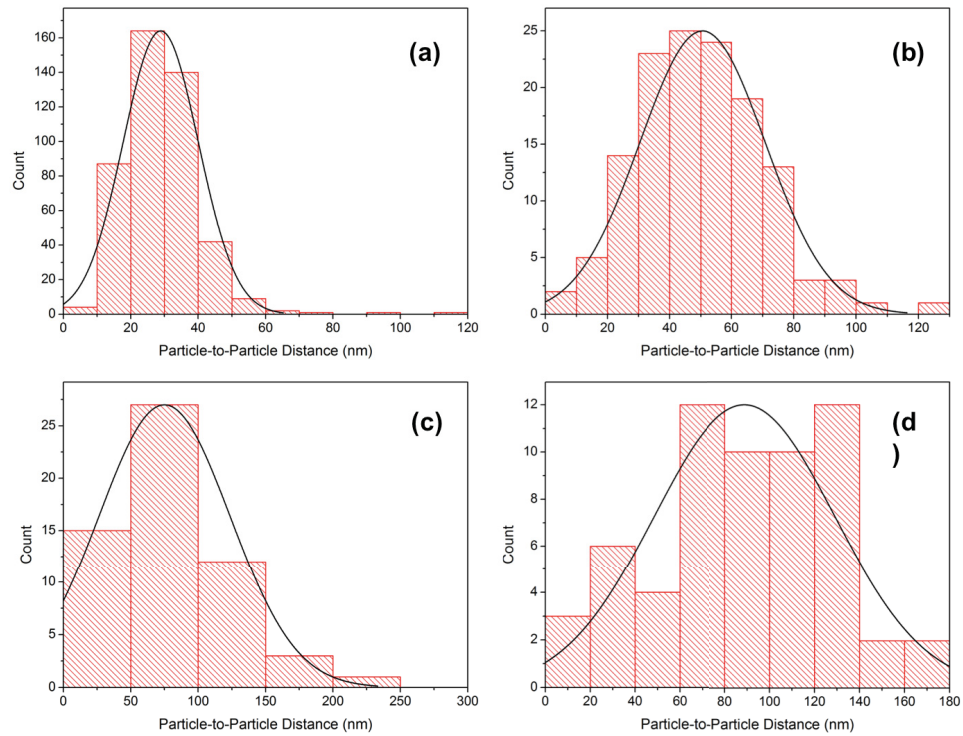
Figure 3.24: Particle to particle distance graphs for (a) sample 10, (b) sample 12, (c) sample 14, and (d) sample 16. All annealed at 500°C

3.6 Ultraviolet-Visible Spectroscopy

3.6.1 Bulk vs. Nanostructured Gold Absorption Spectrum. In order to effectively contrast the plasmon resonance displayed with nanostructured gold, the absorption spectra of bulk gold was taken, and as can be seen from Figure 3.25, there is a radical difference from the nanostructured gold synthesized in this study, resulting in an almost inverse relationship. The nano-patterned gold exhibits a strong absorption between 500 nm and 600 nm, during the activation of the plasmon resonance effect, while the bulk gold does not begin to absorb until much later in the visible spectrum.

60

UV-Vis Absorption Spectra: Bulk Vs Nanostructure Gold
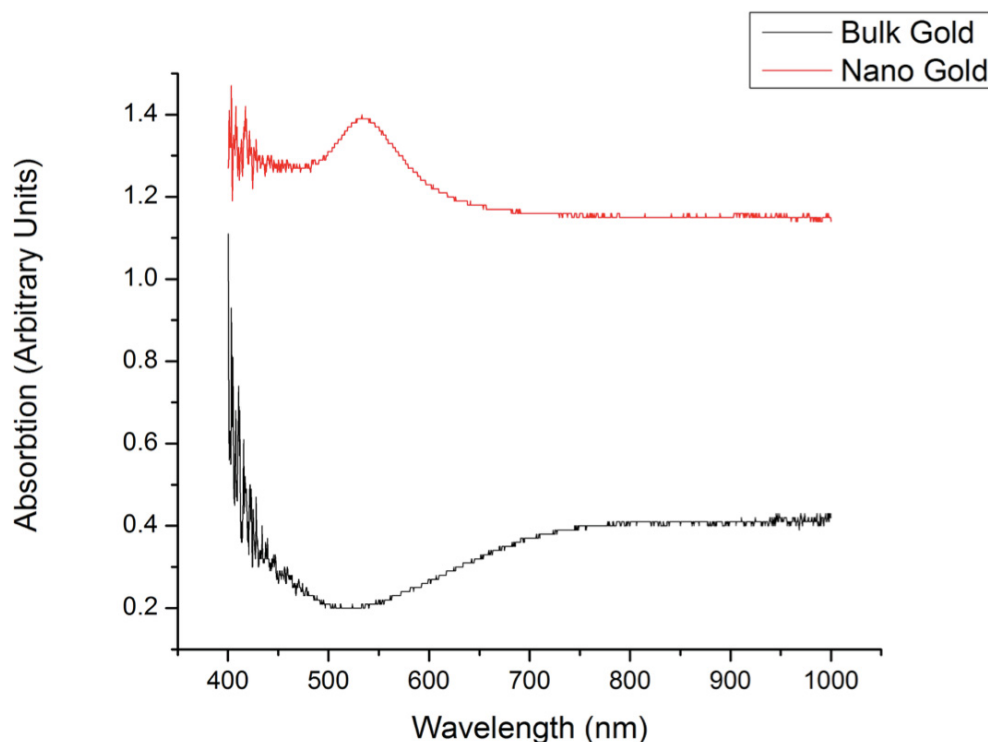
Figure 3.25: Sample 16 pre and post anneal treatment, modeling bulk vs. nanostructured gold ultraviolet-visual spectroscopy absorption spectra.

3.6.2 One Hour Bake (300°C) Comparison. Seen below in Figure 3.26, the ultraviolet visual absorption spectrum of samples 2, 3, 6, 8, all heated at 300°C, presents some interesting results. Samples 2, 4, and 6 all display a strong LSPR peak between 500 nm and 600 nm, while the more heavily coated sample 8 trends toward a more bulk trend, activating around 650 nm. However, even this sample exhibits a decline in absorption after 700 nm, distinguishing it from its bulk counterpart. Samples annealed at 300°C also display more variety than those annealed at 500°C, with some degree of LSPR frequency shift occurring between sample 2 and sample 8.

300° C Anneal UV-VIS Absorption Spectra Comparison
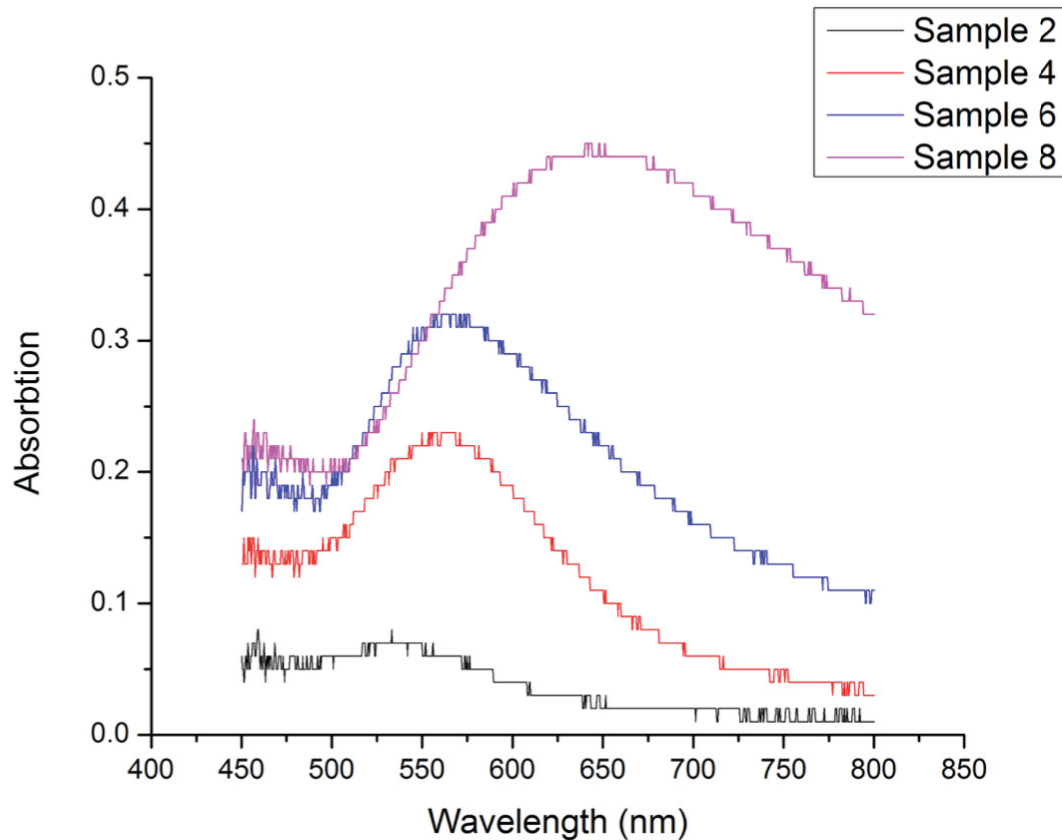
Figure 3.26: Ultraviolet visual absorption spectrum of samples 2, 4, 6, and 8, showcasing spectral change as a direct consequence of synthesis method.

3.6.3 One Hour Bake (500°C) Comparison. Samples 10, 12, 14, and 16, shown below in Figure 3.27, are identical to the previous set except for one detail. These samples were baked for one hour in 500°C, as opposed to 300°C. This change shows itself in several interesting ways. First, a higher temperature seems to play a role in overall absorption intensity. In each otherwise similar sample, the intensity of the absorption decreases due to this increase, elucidating annealing dynamics to a much greater degree. As previously mentioned, there are two different potential processes that can occur during the annealing of nano-structured samples, melting and sublimation.

Traditionally an increased amount of absorption intensity can be attributed to greater amount of material present to absorb. With this attribute in mind, it is possible to surmise that some degree of sublimation occurs during the 500°C anneal, resulting in the documented decrease in absorption intensity. This inference is further supported if one examines the spectra for sample 16 and contrasting with sample 8. Both samples were deposited under the same growth conditions, and annealed at separate temperatures. This one difference in synthesis technique resulted in a drastic shift in light absorption as well as absorption range, indicating less bulk behavior in sample 16. This in turn supports sublimation as an annealing dynamic, corroborating similar conclusions drawn from AFM and XRD results.
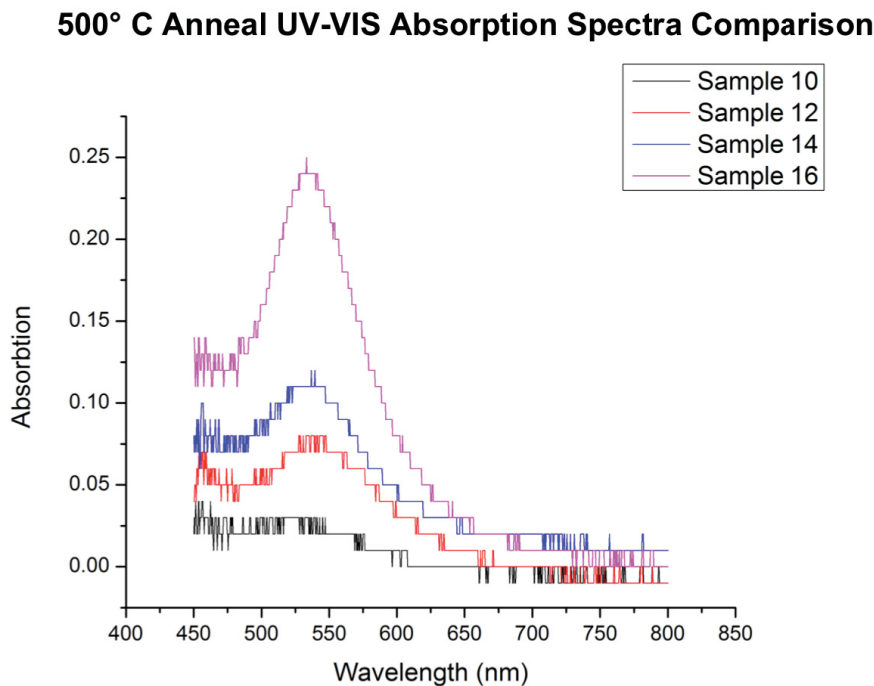
Figure 3.27: Ultraviolet visual absorption spectrum of samples 10, 12, 14, and 16, showcasing spectral change as a direct consequence of synthesis method

3.6.4 UV-VIS Spectra Graphical Comparison: To accurately compare and contrast activation spectrums as well as intensity of light absorbed for each different sample, origin software was utilized to integrate the area under each curve as well to determine the minimum and maximum wavelengths of absorbed light. These values were collected and tabulated in Table 3.2 below.

Table 3.2: Localized surface plasmon resonance activation spectrums and intensity of light absorption

Sample Number	Area Under Curve	LSPR Activation Spectrum (nm)
2	.9	95.502
4	13.1	146.358
6	15.8	194.928
8	49.7	470.938
10	30.4	157.187
12	.9	70.385
14	1.4	80.337
16	7.3	91.875

As shown above, samples with a larger average particle size tend to have both a larger LSPR activation spectrum as well as the ability to absorb more light intensity. An increase in material mass easily accounts for the larger amount of light absorption, but the larger activation spectrum is more difficult to explain. The most probable explanation arises if one inspects the particle diameter comparison shown in previous sections. While there is an overall tendency toward a larger particle size prevalent in the data, in most

cases if larger particles have formed, there is also a presence of particles with smaller sizes as well. This means that the distribution of MNPs is capable of absorbing light at wavelengths corresponding to a variety of differently sized particles, leading to a larger activation spectrum. Ideally, these substrates can be utilized to be more compatible with a wider variety of incident light wavelengths, allowing the SERS effect to be activated more readily without specialized equipment.

3.7 Raman Spectroscopy

After gathering Raman spectra of R6-G from samples 2, 4, 6, and 8, results were compiled and presented in figure 3.28, seen below. Of particular interest is the spectral region between 200 cm$^-$1 and 800 cm^{-1}, as this area contains the most significantly enhanced Raman shift peaks within the data set. This result is somewhat perplexing, as all phonon modes within the material should be experiencing the same boost via the oscillating plasmons, and thus the sample seems to be experiencing some degree of preferential enhancement. This could be caused by some form of defect site present within the gold nanoparticles, attaching to certain portions of the molecule. However, regardless of preference of enhancement site, a side by side comparison of a single peak will provide a strong indication of SERS boost. Samples 4 and 6, those with smaller particle size and spacing, clearly experienced a larger SERS effects than the others, indicating a preference toward coupled plasmonic interactions. Sample 8, interestingly, experienced almost no boost effect whatsoever. Although the morphology of the particles in sample 8 is admittedly less traditionally useful for SERS than the others, the true reason for this absence of electromagnetic boost is the frequency requirement for its

plasmon resonance condition. The absorbance spectra for sample 8 points to its LSPR

being activated after 600 nm, a requirement not met by the 532 laser utilized in this

Raman study. Thus, the SERS effect was not activated, and little intensity boost was

experienced.

Figure 3.28: Raman spectra of Rhodamine 6-G comparison of 300°C anneal treated samples 2, 4, 6, and 8. Showcasing Raman boost when compared to spectra gathered on uncoated quartz.

The R6-G Raman spectras in Figure 3.29,compiled for the samples annealed at

500°C, continue to display the traditional Raman curve for all samples in the set save for

12. This can be explained by the irregular spacing of the gold nanoparticles displayed in the topographical and phase diagrams for the sample.

500°C Anneal Raman Spectra Comparison: Rhodamine 6-G
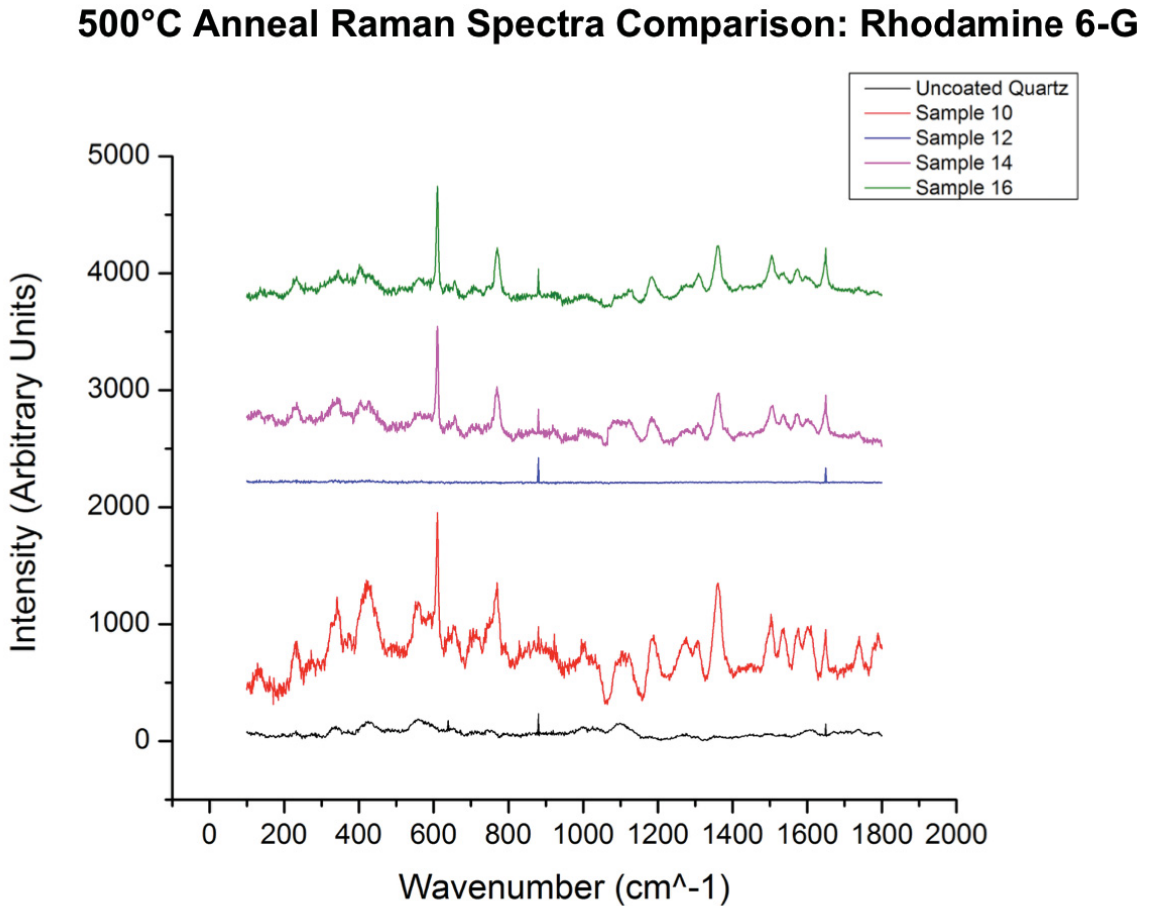
Figure 3.29: Raman spectra of Rhodamine 6-G comparison of 500°C anneal treated samples 10, 12, 14, and 16. Showcasing Raman boost when compared to spectra gathered on uncoated quartz.

Summarized in Table 3.2, the Raman intensity boosts experienced by the various substrates rest primarily between roughly 100-200 times the original Raman intensity detected on uncoated quartz. While surface enhanced Raman substrates patterned through nanolithography and other more precise methods typically experience boosts many times

this magnitude, these less intense substrates can still be made useful in markets where

only a modest boost is necessary.

Table 3.3: Raman intensity boost for quartz samples

Sample Number	Top Peak Intensity	Bottom Peak Intensity	Calculated Peak Intensity	SERS Intensity Boost
2	1103	143.1	959.7	96
4	2216	381.2	1834.3	183
6	2169	561.7	1607	161
8	176	134.4	41.3	4
10	1650	426.9	1223.5	122
12	N/A	N/A	N/A	N/A
14	1033	133.4	899.6	90
16	1041	123.1	918.1	92
Uncoated Quartz	112	102	10	N/A

CHAPTER 4: CONCLUSIONS

In summary, during the course of this study gold nano particles were grown on 16 different substrates under varying parameters in order to ascertain both the viability of sputter vapor deposition in the growth of surface enhanced Raman substrates as well as the optimum parameters for synthesizing such a device. Samples were characterized through a wide variety of techniques such as scanning electron microscopy, atomic force microscopy, x-ray diffraction, Raman spectroscopy, ultraviolet visual spectroscopy, as well as various types of analysis software. During this investigation, surface features were determined and mapped to synthesis parameters, spectroscopic behaviors were correlated with morphology, and optimal growth and use parameters were determined.

4.1 Substrate Growth Parameters and Particle Morphology

Surface features mapped for samples under examination, summarized in Table 4.1, provide a comprehensive list of particle diameter, height, particle-to-particle distance, and surface roughness. This allows for a side-by-side comparison of growth parameters and features produced. For quick reference, odd numbered samples have been synthesized on silicon substrate and even numbered samples on quartz. Samples grown on silicon do not have values for either particle height or roughness, due to the fact that they were characterized via scanning electron microscopy, which does not allow for that data to be analyzed.

Table 4.1: Particle morphology summary

Sample Numbers	Average Particle Diameter (nm)	Average Particle Height (nm)	Average Interparticle Distance (nm)	Particle Roughness (nm)
1	17.02	N/A	30.52	N/A
2	21.66	3.32	26.13	0.329
3	13.29	N/A	29.52	N/A
4	38.08	14.98	48.20	0.611
5	18.37	N/A	36.81	N/A
6	37.09	46.64	77.12	3.14
7	45.36	N/A	72	N/A
8	151.93	41.52	139.84	2.62
9	15.91	N/A	24.35	N/A
10	25.36	3.33	28.90	0.448
11	50.76	N/A	125.18	N/A
12	41.93	14.47	50.61	0.408
13	52.14	N/A	75.53	N/A
14	74.38	41.50	75.02	1.33
15	53.31	N/A	86.03	N/A
16	92.77	38.27	88.76	0.504

4.1.1 Effect of Initial Film Thickness. By varying both sputter time and amperage, initially deposited gold film thickness was scaled up sample by sample through samples 1-8, and again through samples 9-16. This increase manifests itself most strongly within the first sample set (sample 1-8), scaling up every surface analysis parameter as film thickness increases. This change is especially evident within surface roughness, jumping from .329-2.62 nm from sample 2 to sample 8. While samples 9-16 do not exhibit this trend as strongly, due in part to the difference in annealing temperature, they also display the same increase in all parameters as film thickness scales up. This scalability makes sense, as with more initial material, there should be larger,

70

taller particles, and they should display an increased roughness, as there is a larger area to take into account. Particle to particle distance follows this trend as well, as with more gold sites to be drawn to, mobile Au atoms will not have to migrate as far to nucleate, resulting in larger, more spaced agglomeration of particles.

4.1.2 Effect of Annealing Temperature. Particle to particle distance and surface roughness display the strongest difference based on annealing temperature. When compared side-by-side, samples within set one typically displays a higher particle surface roughness than those in sample set two. Considering the traditional use for annealing treatment, promotion of film uniformity, it is conjectured that the higher temperature of the second annealing parameter begins to smooth out height discrepancies within the nanoparticles, resulting in a lower roughness on average. The increased thermal excitation caused by this anneal also explains the increase in particle to particle distance, as the migratory Au atoms have more of range to travel in and locate central nucleation sites, rather than create smaller more numerous particles. There does not seem to be an appreciable difference across the sample sets in particle diameter or height, although the transition to larger particle size does seem to occur faster within the 500°C sample set.

4.1.3 Effect of Substrate. Substrate choice, quartz or silicon, does not seem to present a large factor in terms of growth kinetics, but there does seem to be a stronger prevalence toward smaller particle size and more ordered growth on the silicon. This could be attributed to several different possible reasons, among them differing underlying crystal structures, as well as varying parameters for wettability of the different substrates. Either of these differences could potentially alter the growth energetics of the system enough to influence particle agglomeration.

4.2 Morphology Effects on Localized Surface Plasmon Resonance Condition

Modeled below in Figure 4.1, the wavelength of light required for the localized surface plasmon resonance condition displays a certain degree of correlation with the physical morphology of the gold nanoparticles, most predominantly in terms of surface roughness. While diameter, particle to particle distance, and particle height all seemed to be related in some fashion, with the overriding general trend being a larger measurement leading to a higher resonance wavelength, surface roughness seems to bear a much stronger connection to the actual nanoparticle excitation than any other physical feature, with a larger surface roughness rating corresponding to a larger wavelength of light being required to manifest the plasmonic interaction.
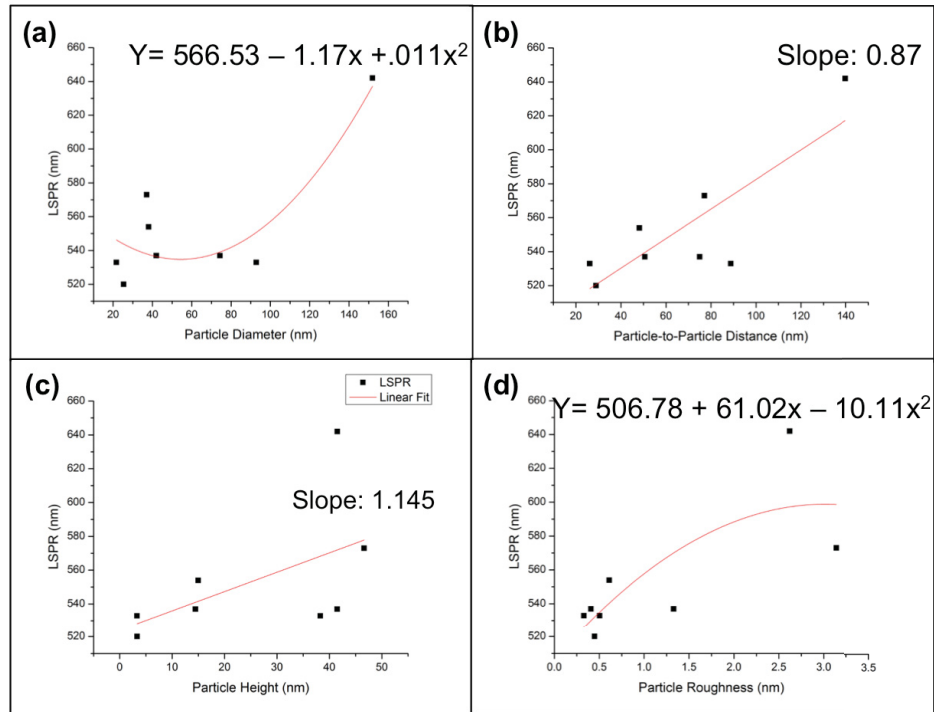
Physical Morphology Effects on the LSPR

Figure 4.1: LSPR dependence on morphology parameters (a) particle diameter, (b) particle-to-particle distance, (c) particle height, and (d) particle roughness

Due to the exacting nature of Raman spectroscopy, most spectroscopic setups only posses two or three different laser wavelengths, tuning the plasmon resonance condition required for SERS to a specified wavelength represents a powerful tool in the continuing search for ever more sensitive detection techniques. The Raman spectrtoscopy system used for this investigation for example, comes equipped with a 532 nm green laser for material analysis. According to the LSPR analysis conducted, this system would benefit from the use of SERS substrates patterned with gold nanoparticles possessing a low surface roughness ratio, under 0.5 nm, and smaller particle size and particle-to-particle distance.

4.3 Morphology Effects on Raman Signal Enhancement

Correlated and combined below in Figure 4.2, Raman intensity boost exhibits a much stronger dependence on particle diameter and spacing than the plasmon resonance condition, with smaller distances for both leading to a larger Raman intensity boost. Particle height and roughness do not seem to be as large a factor in boost intensity as would be expected, indicating that perhaps a larger sample size might be necessary in order to obtain a clearer picture of optimum morphology for interaction. In any case, it can be conclusively stated that gold SERS substrates with smaller particle sizes spaced closer together are much more conducive to achieving a Raman boost than those with larger, more agglomerated particles, undoubtedly due to the coupled plasmon interactions that occur between two oscillating plasmons when particles overlap.

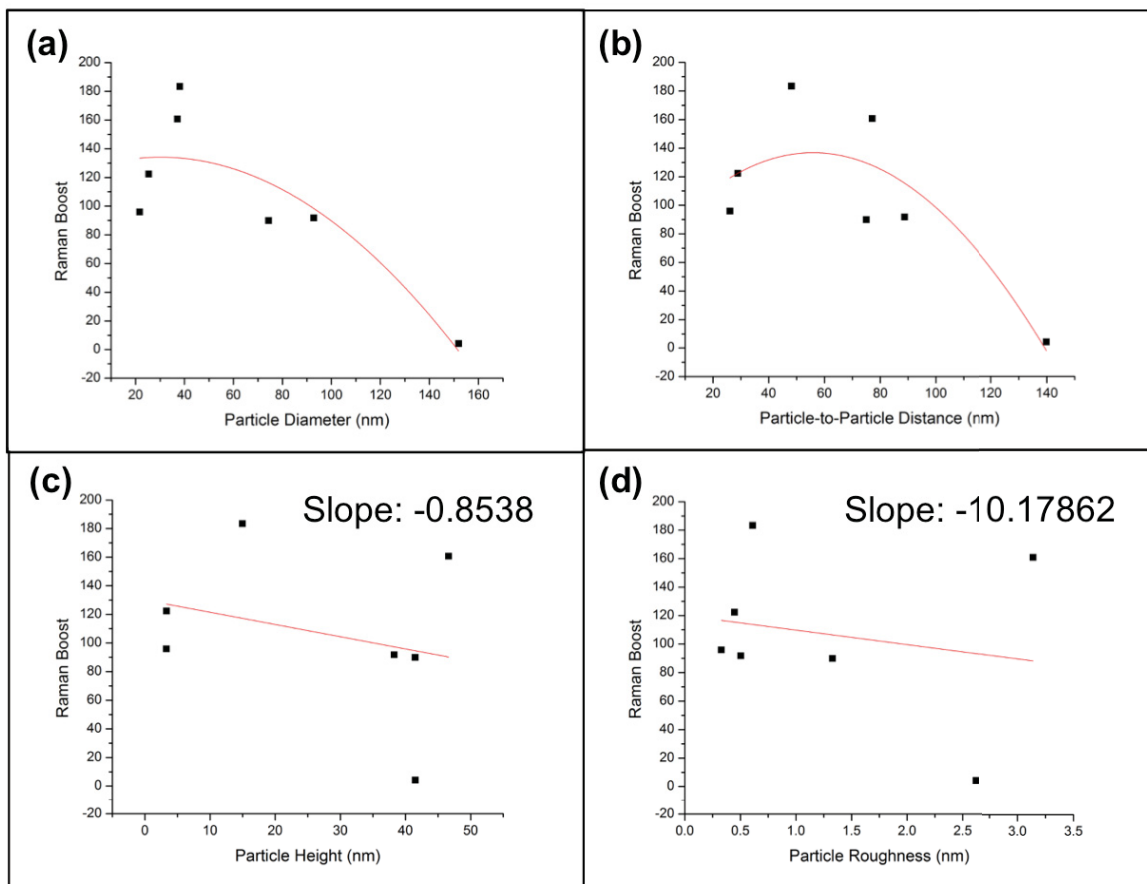# Physical Morphology Effects on Raman Intensity Boost

Figure 4.2: Raman intensity enhancement dependence on morphology parameters (a) particle diameter, (b) particle-to-particle distance, (c) particle height, and (d) particle roughness.

REFERENCES

1. Pool Jr., C. P., Owens, F. J. *Introduction to Nanotechnology.* Hoboken, New Jersey: John Wiley and Sons Inc (2003).

2. H. Chang, H. Wu. Graphene-Based Nanomaterials: Synthesis, Properties, and Optical and Optoelectronic Applications. Advanced Functional Materials **23**, 1984-1997 (2013).

3. K. Sobolev, M. F. Gutierrez. How Nanotechnology Can Change the Concrete World. *American Ceramic Society Bulletin* **84**, No 10 14-18 (2005).

4. S. Zeng, K. Yong, I. Roy, X. Dinh, X. Yu, F. Luan. A Review on Functionalized Gold Nanoparticles for Biosensing Applications. *Pasmonics* **6**, 491-506 (2011).

5. I. Petrov, P. B. Barna, L. Hultman, J.E. Greene. Microstructural Evolution During Film Growth. *Journal of Vacuum Science A* **21**(5), S117-S128 (2003).

6. W. D. Callister Jr. D. G. Rethwisch. *Materials Science and Engineering: An Introduction.* Hoboken, New Jersey: John Wiley and Sons Inc (2010).

7. B.J.Y. Tan, C.H. Sow, T.S. Koh, K.C. Chin, A.T.S. Wee, C.K. Ong. Fabrication of Size-Tunable Gold Nanoparticles Array with Nanosphere Lithography, Reactive Ion Etching, and Thermal Annealing. *Journal of Physics Chemistry B* **109**, 11100-11109 (2005).

8. Y. Ding, F. Fan, Z. Tian, Z. L. Wang. Sublimation-Induced Shape Evolution of Silver Cubes. *Small Journal* **5**, No 24 2812-2815 (2009).

9. G. Gouadec, P. Colomban. Raman Spectroscopy of Nanomaterials: How Spectra Relate to Disorder, Particle Size and Mechanical Properties. *Progress in Crystal Growth and Characterization of Materials, Elsevier* **53**, 1-73 (2007).

10. Swartz, M. *Analytical Techniques in Combinatorial Chemistry*. 65-77 (Marcel Dekker, 2000).

11. C. L. Haynes, A. D. McFarland, R. P. Van Durne. Surface–Enhanced Raman Spectroscopy. *American Chemical Society A*, 338-346 (2005).

12. P. L. Stiles, J. A. Dieringer, N. C. Shah, R. P. V. Duyne. Surface-Enhanced Raman Spectroscopy. *Annual Review of Analytical Chemistry* **1**, 601-626 (2008).

13. C.W. Chu, F. Chen, J. Shulman, S. Tsui, Y.Y. Xue, W. Wen, P. Sheng. A negative dielectric constant in nano-particle materials under an electric field at

very low frequencies. *Strongly Correllated Electron Materials: Physics and Nanoengineering* **5932**, 1-9 (2005).

14. K.A. Willets, R.P. Van Duyne. Localized Surface Plasmon Resonance Spectroscopy and Sensing. *Annual Review Physical Chemistry* **58**, 267-297 (2007).

15. E. Ozbay. Plasmonics: Merging Photonics and Electronics at Nanoscale Dimensions. *Science* **311**, 189-193 (2006).

16. S. J. Lee, Z. Guan, H. Xu, M. Moskovits. Surface-Enhanced Raman Spectroscopy and Nanogeometry: The Plasmonic Origin of SERS. *The Journal of Physical Chemistry Letters C* **111**, 17985-17988 (2007).

17. M. Fan, G.F.S. Andrade, A. G. Brolo. A Review on the Fabrication of Substrates for Surface Enhanced Raman Spectroscopy and Their Applications in Analytical Chemistry. *Analytica Chemica Acta* **693**, 7-25 (2011).

18. H. Wang, C. Liu, S. Wu, N. Liu, C. Peng, T. Chan, C. Hsu, J. Wang, Y. Wang. Highly Raman-Enhancing Substrates Based on Silver Nanoparticle Arrays with Tunable Sub-10 nm Gaps. *Advanced Materials* **18**, 491-495 (2006).

19. U. Helmersson, M. Lattemann, J. Bohlmark, A.P. Ehiasarian, J.T. Gudmundsson. Ionized Physical Vapor Deposition (IPVD): A Review of Technology and Applications. *Think Solid Films* **513**, 1-2 and 1-24 (2006).

20. V. Amendola, M. Meneghetti. Size Evaluation of Gold Nanoparticles by UV-vis Spectroscopy. *Journal of Physics Chemistry C* **113**, 4277-4285 (2009).

21. G.E. Lloyd. Atomic Number and Crystallographic Contrast Images with the SEM: A Reivew of Backscattered Electron Techniques. *Mineralogical Magazine* **51.359**, 3-19 (1987).

22. M. D. Abramoff. Image Processing with ImageJ. *Biophotonics International*. 1-7 (2004).

23. A Ryland. X-Ray Diffraction. *Journal of Chemical Education* **35**, 80-83 (1958).

24. A. L. Patterson. The Scherrer Formula for X-Ray Particle Size Determination. *Physical Review* **56**, 978-982 (1939).

25. B. Akbari, M. P. Tavandashti, M. Zandrahiml. Particle Size Characterization of Nanoparticles-A Practical Approach. *Iranian Journal of Materials Science and Engineering* **8**, 48-56 (2011).

26. F. J. Giessibl. Advances in Atomic Force Microscopy. *Reviews of Modern Physics* **75**, 949-983 (2003).

27. C. Y. Poon, B. Bhushan. Comparison of Surface Roughness Measurements by Stylus Profiler, AFM and Non-Contact Optical Profiler. *Wear* **190**, 76-88 (1995).

28. A. M. Michaels, M. Nirmal., L.E. Brus. Surface Enhanced Raman Spectroscopy of Individual Rhodamine 6G Molecules on Large Ag Nanocrystals. *Journal of the American Chemical Society* **121**, 9932-9939 (1999).

29. Y. Liu, C Yu, S. Sheu. Low Concentration Rhodamine-6G Observed by Surface-Enhanced Raman Scattering on Optimally Electrochemically Roughened Silver Substrates. *Journal of Materials Chemistry* **16**, 3546-3551 (2006).

30. E. C. L. Ru, E. Blackie, M. Meyer, P.G. Etchegoin. Surface Enhanced Raman Scattering Enhancement Factors: A Comprehensive Study. *Journal of Physical Chemistry C* **111**, 13794-13803 (2007).